A Comprehensive Approach to the Analysis of Contrast Enhanced Cardiac MR Images

Anja Hennemuth*, Achim Seeger, Ola Friman, Stephan Miller, Bernhard Klumpp, Steffen Oeltze, and Heinz-Otto Peitgen

Abstract—Current magnetic resonance imaging (MRI) technology allows the determination of patient-individual coronary tree structure, detection of infarctions, and assessment of myocardial perfusion. Joint inspection of these three aspects yields valuable information for therapy planning, e.g., through classification of myocardium into healthy tissue, regions showing a reversible hypoperfusion, and infarction with additional information on the corresponding supplying artery. Standard imaging protocols normally provide image data with different orientations, resolutions and coverages for each of the three aspects, which makes a direct comparison of analysis results difficult. The purpose of this work is to develop methods for the alignment and combined analysis of these images. The proposed approach is applied to 21 datasets of healthy and diseased patients from the clinical routine. The evaluation shows that, despite limitations due to typical MRI artifacts, combined inspection is feasible and can yield clinically useful information.

Index Terms—Cardiac magnetic resonance (MR), late enhancement, myocardial perfusion.

I. INTRODUCTION

AS coronary artery disease (CAD) is one of the main causes of death in the western world, diagnosis and therapy planning are tasks of high importance. Coronary artery plaque causes stenoses, which may lead to hypoperfusion of the dependent myocardial tissue. Continuous perfusion defects may cause necrosis which in turn decreases myocardial function and may lead to a heart failure. According to this so-called *ischemic cascade*, disturbances due to stenoses become apparent in myocardial perfusion prior to myocardial function [1]. The states of myocardial tissue that frequently appear in CAD patients [2] are listed in Table I. Since only viable hypoperfused tissue can benefit from reperfusion therapy, the state of tissue is an important parameter for therapy decisions.

CAD patients tend to develop plaque, which leads to a narrowing of the vessel lumen at different positions in the coronary tree (multivessel CAD), but not all of these stenoses influence the myocardial perfusion. Thus, in addition to the assessment

Viability	Term	Description
Viable	Normal	Healthy myocardium with normal perfusion and function
	Stunned	Normally perfused myocardium with a dysfunction that is persistent for max. 2 weeks after acute ischemia
	Hypoperfused	Hypoperfused myocardium with normal function
	Hibernating	Hypoperfused dysfunctional myocardium
Non-viable		Necrotic tissue with neither perfusion nor function

of the coronary arteries the following tasks are important for therapy planning:

1) the detection of hypoperfused viable myocardial tissue;
2) the correlation between the hypoperfused viable tissue and the supplying vessel.

The knowledge about this correlation is crucial for the decision on the best available therapy, which could be surgical and catheter-based interventions as well as pharmacological therapy. As magnetic resonance imaging (MRI) provides a noninvasive and radiation-free means to inspect coronary arteries, myocardial infarction, function and perfusion dynamics, it is recommended for these diagnostic tasks by the American Heart Association (AHA) and the American College of Cardiology (ACC). The image data acquired for CAD assessment with contrast enhanced cardiac MRI normally consist of the following.

- Two perfusion sequences acquired under pharmacological stress and at rest, depicting the wash-in and wash-out of the contrast agent during its first pass through the myocardium.
- Late enhancement image slices showing the myocardial infarction as a hyperenhanced area due to the increased distribution volume of the contrast agent in necrotic tissue [3].
- An optional whole-heart volume dataset consisting of high-resolution axial slices for coronary tree analysis.

The differentiation between normally perfused, hypoperfused, and nonviable tissue (task 1) can be made by a comparison of infarction and perfusion information. Reversibly defective tissue shows a perfusion defect but no infarction. Clinical studies have shown the importance of a classification that differentiates healthy, necrotic, and viable hypoperfused myocardium occurring in the so-called peri-infarct zone [4], [5]. Therefore, an advanced late enhancement analysis [5] as well as
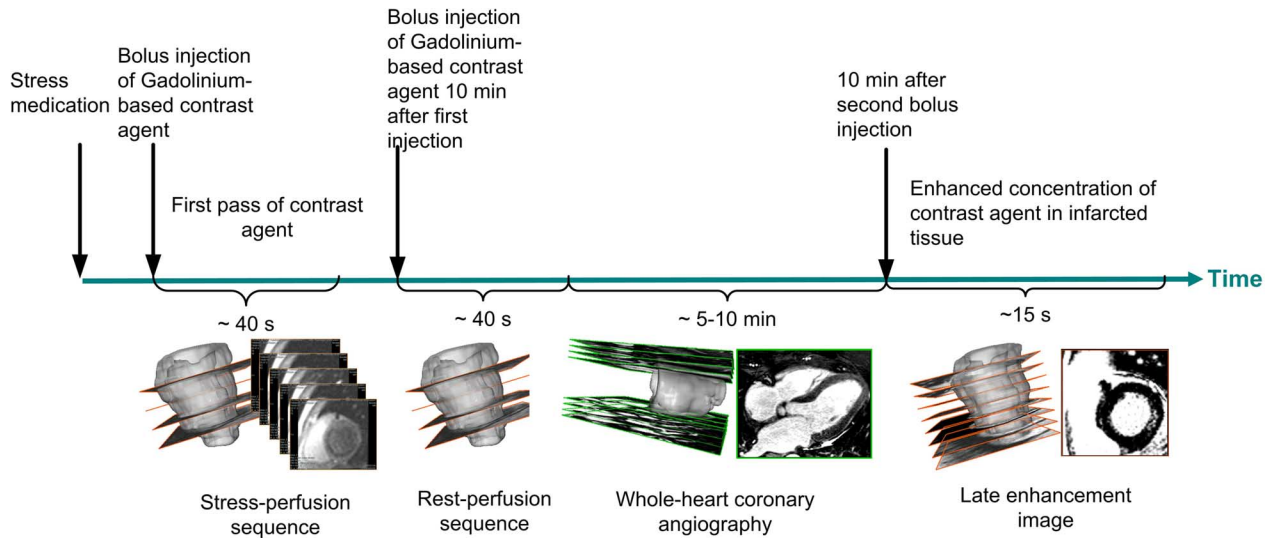
Fig. 1. Image sets for contrast enhanced cardiac MR perfusion analysis.

the combined inspection of perfusion and delayed enhancement images [6] have been proven suitable.

To address task 2, the spatial relation between the reversibly defective tissue area and the coronary arteries has to be inspected. The AHA proposes a standardized model for this relationship [7], but studies have shown that it is not applicable in all cases [8], especially in patients with pathological changes and previous vascular interventions. Hence, a patient-individual analysis should be performed.

The image processing that must be performed can be grouped into alignment and analysis problems.

- Image alignment:
  — spatial alignment of the image slices in the late enhancement dataset;
  — temporal alignment of the image slices within the perfusion sequences;
  — alignment of the whole-heart image, the late enhancement image, and the perfusion sequences.
- Image analysis:
  — detection of the coronary artery tree in the whole-heart volume image;
  — segmentation of infarcted tissue regions in late enhancement images;
  — identification of hypoperfused tissue regions in the perfusion image sequences.

The purpose of this work is to develop and compile methods that solve these problems. To evaluate the applicability of the developed methods, 21 datasets were processed. Two radiologists assessed the results with respect to consistence with the clinical findings based on other examinations and with regard to the benefit of a combined analysis.

The outline of this paper is as follows. In Section II, we describe the special characteristics of the contrast enhanced cardiac MR images. Section III gives an overview of existing and proposed methods for the alignment of sparse cardiac images. In Section IV, we discuss existing image analysis approaches and present new techniques. The results are presented in Section V and discussed in Section VI. Section VII contains a summary of

the paper as well as the final conclusions. Algorithmic details on applied methods are described in the Appendix.

II. IMAGE DATA

Contrast enhanced cardiac MR image data consist of different images for morphological and dynamic analysis. Typical acquisition protocols contain two perfusion sequences where images are acquired in short-axis orientation under pharmacologically induced stress and at rest, and a set of late enhancement images containing a stack of short-axis slices and optional long-axis slices. Recent developments in MRI acquisition technology also allow acquisition of coronary angiograms, which are suitable for inspecting the coronary tree [9]. Fig. 1 shows a clinical image acquisition protocol for contrast enhanced MR analysis of myocardial perfusion.

- **Perfusion Images**: Perfusion images are acquired after Gadolinium contrast agent bolus injection over 40–60 consecutive heartbeats and they show the contrast agent's first pass through the myocardium. Three to four short-axis slices with about 8 mm thickness, an in-plane-resolution of 1.7 mm × 1.7 mm, and a gap of up to 10 mm are imaged per heart beat using a balanced SSFP sequence and ECG-triggering. The number of image slices that can be acquired is restricted by the patient-specific heart rate. For the acquisition of the stress-perfusion sequence, the heart rate is increased by pharmacological stress medication. As illustrated in Fig. 2, this means that the application of the same imaging sequence results in image slices that show different contraction phases for perfusion at rest and under stress.
- **Whole-Heart Coronary Angiography**: The whole-heart volume dataset for the inspection of the coronary arteries is acquired with a navigator-gated 3D SSFP sequence with T2 preparation. The acquisition of the slice stack takes around 5 min and the image data consist of axial or coronal slices with about 1.2 mm thickness and a resolution of up to 0.6 mm × 0.6 mm in plane.
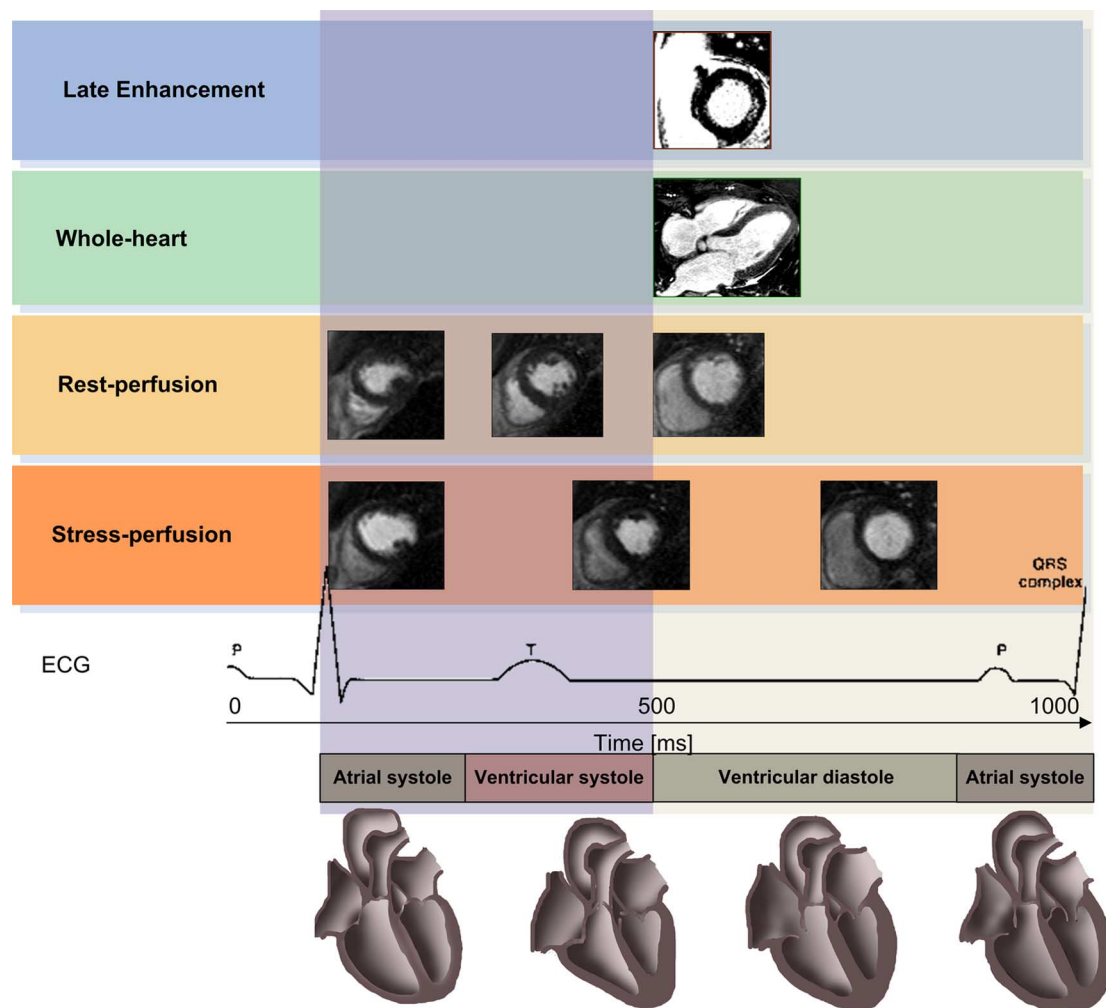
Fig. 2. Temporal position of images in the heart contraction cycle.

- **Late Enhancement Image Slices**: Late enhancement can be imaged 10 min after the contrast bolus injection using an inversion recovery turbo flash sequence. As defective tissue has a higher distribution volume for the Gadolinium-based contrast agent, infarcted areas take on high intensities in the image slices [10], [11]. The acquired slice set usually contains a stack of 5–10 short-axis slices and optional vertical and horizontal long-axis slices. The resolution is about 1.33 mm × 1.33 mm × 5 mm.

Table II shows the sequence parameters that were applied for the acquisition of the examined image datasets. All datasets are acquired with parallel imaging (GRAPPA 2) [12].

As depicted in Figs. 1 and 2, the acquired image sets show different resolutions, slice orientations, and for perfusion images even the temporal position within the cardiac cycle differs. Moreover, displacement of image slices acquired at different time points may occur due to breathing motion. These factors complicate a combined analysis of the images considerably.

III. IMAGE ALIGNMENT

The types of displacement induced by the image acquisition described in the previous sections pose a couple of problems that

TABLE II
SEQUENCE PARAMETERS USED FOR THE IMAGE ACQUISITION

	Perfusion sequence	Late Enhancement image	Whole-heart volume
Repetition / Echo Time [ms]	2.8/1.08	11.04/4.4	4/1.71
Flip angle	15°	30°	90°
Matrix	160x192	192x256	256x173
Field of View [mm²]	340x300	293x360	320x240
Bandwith [Hz/Pixel]	840	140	601
Slice Thickness [mm]	ca. 8	5 - 8	ca. 1.1

need to be solved before a comprehensive combined analysis of all relevant images is possible.

- Alignment of late enhancement image slices in order to correct slice displacements and to allow 3-D image analysis.
- Motion compensation of perfusion image sequences in order to enable the analysis of intensity time courses.
- Matching of the whole-heart volume, the late enhancement image, and the perfusion images to allow a visualization

of spatial relations between healthy, hypoperfused, and infarcted tissue and the supply through the coronary arteries, as described in Section I.

A. Existing Approaches for Image Alignment

1) Spatial Alignment of Slices Belonging to One Image Series: The problem of misalignment between stacked image slices often occurs when these slices are acquired in different heart cycles (see Fig. 2) and in the presence of patient or breathing motion. This effect is seen in cardiac images in general, and there are some approaches to correct the misalignment. The methods proposed by Lötjönen *et al.* [13] and Barajas *et al.* [14] both include long-axis images in the alignment procedure and they apply translation in 3-D to correct the misalignment. The methods differ in the handling of slice distances and the applied optimizer. Rotational motion is neglected in both approaches.

2) Temporal Alignment of Perfusion Sequences: To assure spatial correspondence of regions of interest, the displacement errors between time frames of the perfusion sequence due to patient motion, contraction, and breathing have to be corrected. For this purpose, classical intensity-based as well as model-based registration methods have been proposed, e.g., based on squared differences [15], normalized cross correlation [16], [17], mutual information [18], [19], and a measure based on gradient strength and direction [20]. Classes of transformations applied for correction are translation [17]–[19], rigid transformations (translation and rotation) [15]–[17], and affine transformations (translation, rotation, shearing, and scaling). More tailored approaches apply model assumptions to support the registration. Such assumptions relate to the shape of the myocardium [18], [20], [21] as well as to the expected temporal intensity course of the imaged regions [22]–[24]. Unlike the late enhancement slices, which are acquired over multiple heart cycles, perfusion slices, which represent one temporal position, are acquired in straight succession. Thus, spatially adjacent slices, which represent one time point, assumingly do not differ strongly regarding their displacement. All the above mentioned approaches perform a per-slice correction which does not account for the long-axis connectivity of the slices at one temporal position.

3) Spatial Alignment to a Reference Dataset: There are only few approaches that address the alignment of different cardiac images. Breeuwer *et al.* assume that the AHA-model segmentations, which divide the myocardium into radial segments within three slices [7], spatially correspond to each other in all inspected images [25], while other strategies consider anatomical landmarks [26] or previously segmented image structures such as the epicardial surface [27], [28]. Since local image information is not taken into account, these methods can only provide relatively imprecise information about spatial relations between image structures from different datasets. The problem of aligning single slices with an image that shows a different coverage, resolution, or even intensity distribution occurs in different application areas. In particular, the application of mutual information was found to be successful for the alignment of short-axis and long-axis images with a preprocedural image volume in MR-guided cardiac interventions [29].
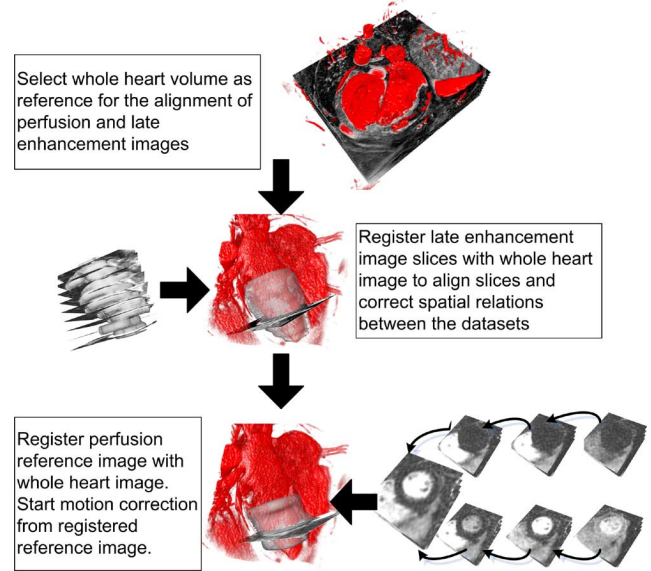

Fig. 3. Workflow of image preprocessing for a combined analysis of coronary angiography, late enhancement, and perfusion.

B. Proposed Methods for Image Alignment for Advanced Perfusion Analysis

A major problem in the analysis of late enhancement and perfusion images is the relatively low spatial resolution and the related partial volume effects. Additional smoothing is introduced by interpolation when spatial transformations are applied. We therefore try to solve the intraimage and interimage alignment problems described above with a minimum of transformations and apply the workflow depicted in Fig. 3. The whole-heart dataset serves as reference, because it shows the highest image information density and it is already aligned due to the navigator acquisition technique. Furthermore, it is acquired after the first perfusion sequence and before the late enhancement image. Late enhancement patterns may already be present, but not yet at full strength, meaning that the intensity distribution is suitable as reference.

1) Alignment of Late Enhancement Slices: To correct slice misalignment in the late enhancement image, the image slices are matched separately onto the whole-heart image volume. Images are acquired in the same cardiac contraction phase. Any displacement between the images is therefore caused by patient- or breathing-motion. This displacement can be described by rigid transformations, which are volume preserving. Thus, one can compare the results with those of other applications. When matching a single slice I_{LE_i} of the late enhancement image I_{LE} with the whole-heart image I_{WH}, only the overlapping image parts $I'_{\mathrm{LE}_i}, I'_{\mathrm{WH}}$ have to be compared. That is, for every evaluation step, the computation of the similarity measure is restricted to the intersection of the domains $D^t_{\mathrm{LE}_i} \cap D_{\mathrm{WH}}$, where $D^t_{\mathrm{LE}_i}$ is the domain of the transformed late enhancement slice i and D_{WH} is the domain of the whole-heart volume. To find a suitable similarity measure $\mathcal{S}$ we evaluate the following similarity measures [13], [14], [29].

- **Normalized Cross Correlation (NCC)**

$$\mathcal{S}\left(I^t_{\mathrm{LE}_i}, I_{\mathrm{WH}}\right) = \mathrm{NCC}\left(I^{t'}_{\mathrm{LE}_i}, I'_{\mathrm{WH}}\right) \qquad (1)$$
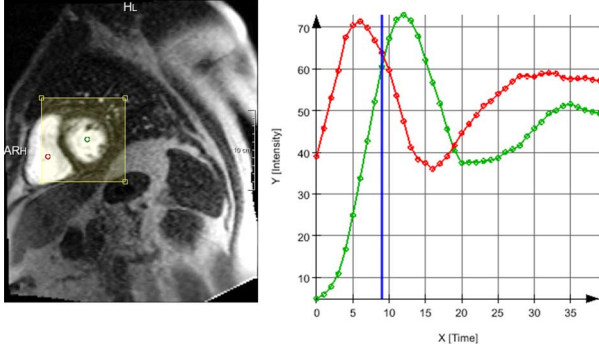
Fig. 4. Interactive preprocessing steps. The yellow box shows the user-defined subimage at the reference time point t_M, which is determined by the intersection of the curves in the diagram on the right. The colors of the intensity curves correspond to the markers defining the subjacent image regions in the left image.
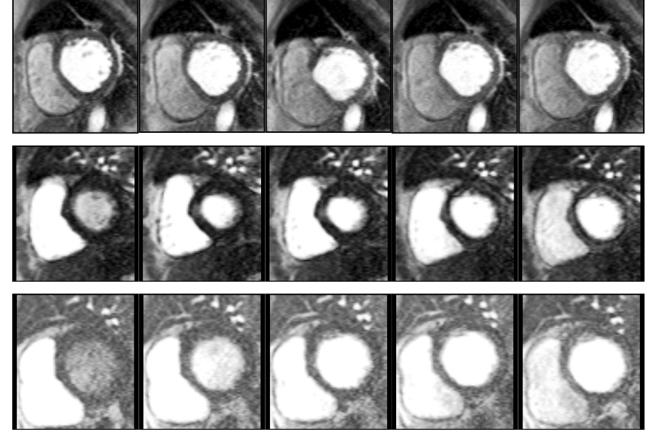

Fig. 5. Different kinds of motion in perfusion sequences: The upper row shows five consecutive time frames of a stress perfusion sequence with out-of-plane motion (case 7: the left ventricular outflow tract appears in the third image). In the middle sequence (case 10) the myocardium changes its thickness by contraction and the lower column (case 1) shows displacement from breathing motion.

with

$$\text{NCC}(I_1, I_2) = \frac{\text{Cov}(I_1, I_2)^2}{\text{Var}(I_1)\text{Var}(I_2)}. \quad (2)$$

• **Normalized Mutual Information (NMI)**

$$\mathcal{S}\left(I_{\text{LE}_i}^t, I_{\text{WH}}\right) = \text{NMI}\left(I_{\text{LE}_i}^{t'}, I_{\text{WH}}'\right) \quad (3)$$

with

$$\text{NMI}(I_1, I_2) = \frac{h(I_1) + h(I_2)}{h(I_1, I_2)}. \quad (4)$$

with

$$I_{\text{LE}_i}^{t'} = I_{\text{LE}_i}^t|_{D_{\text{LE}_i}^t \cap D_{\text{WH}}} \quad (5)$$

$$I_{\text{WH}}' = I_{\text{WH}}|_{D_{\text{LE}_i}^t \cap D_{\text{WH}}} \quad (6)$$

Both methods have the term *normalized* in their name. Regarding NCC this refers to the use of $\text{Var}(I)$ to achieve scale invariance, whereas for NMI the integration of the marginal entropies $h(I)$ provides a certain robustness to changes of the overlapping regions $D_1^t \cap D_2$ due to the transformation t [30]. Optimization is performed with the Simplex algorithm by Nelder and Mead [31].

2) Correction of Perfusion Sequences: Perfusion sequences consist of about 40 time points depicting the pass of the contrast agent through right ventricle, left ventricle, and myocardium. As only the myocardial first pass is needed for the derivation of semi-quantitative perfusion parameters (see Section IV-A-3), the motion correction starts from the end of the myocardial baseline. Because of its central temporal position in the perfusion sequence and its intensity distribution, the reference time point is defined as the intersection time of the right and left ventricular intensity curves. Fig. 4 shows a screenshot of the interactive step, where the user has marked two regions in the right and left ventricular blood pool, respectively. The diagram shows the corresponding intensity curves and the determined reference time frame. For registration, this reference image is matched to the whole-heart image dataset with the method that is described for late enhancement slice alignment in the previous section (Fig. 3). As the images are not acquired in the same heart phase,

scaling and shearing are added and thus affine transformations are allowed.

As shown in Fig. 4, the user also defines the region of interest that is to be processed. Time frames that show strong displacement or deformations can also be removed in this step.

As shown by Rogers *et al.* [32], myocardial tissue moves up to 13 mm in the long-axis direction during contraction exceeding the usual slice thickness. Due to the extreme sparseness of the perfusion images, 3-D alignment of the image slices is neither possible nor useful. Therefore, strong outliers are removed from the sequence and the following temporal alignment is performed in 2-D.

The time frame that is aligned with the whole-heart image serves as reference I_R for the motion correction. Diseased patients often tend to show arrhythmias, which can give rise to misalignment due to extrasystolic contractile motion. Fig. 5 shows typical types of motion that frequently appear in perfusion image sequences. The motion correction consists of two steps. First, affine transformations are applied to compensate the displacement and deformation caused by breathing and patient motion. To address slight contractile motion, cubic B-spline transformations are considered in the second phase. We thereto apply a regular grid of four points in both directions, and thus the parameter set X_{ij} to be optimized for an image slice s_i at time point j is composed as follows:

$$X_{ij} = T_x, T_y, R, Sh, S_x, S_y, B_{11}, \ldots, B_{14}, B_{21}, \ldots, B_{44}$$
$$i = 1, \ldots, z_{\max}$$
$$j = t_M, \ldots, t_{\max}$$

T_x, T_y: translation in *x*- and *y*-direction, respectively
R: rotation angle
Sh: shearing
S_x, S_y: scaling
B_{xy}: de Boer point coordinates specifying the
B-spline transformation

To register every slice s_{ij} with its corrected temporal predecessor s_{ij-1}^t the parameter set X_{ij} is optimized by applying the similarity measures S described in Section III-B-1 to the intersection of the corresponding domains D_{ij-1}^t and D_{ij}^t that result

from the application of the transformation T with the parameter sets X_{ij-1}^{opt} and X_{ij}, respectively

$$S\left(s_{ij-1}^{t'}, s_{ij}^{t'}\right)$$

with

$$s_{ij}^{t} = T(X_{ij}, s_{ij})$$
$$s_{ij-1}^{t'} = s_{ij-1}^{t}|_{D_{ij-1}^{t} \cap D_{ij}^{t}}$$
$$s_{ij}^{t'} = s_{ij}^{t}|_{D_{ij-1}^{t} \cap D_{ij}^{t}}$$

As described in Section II, perfusion slices are acquired over the course of one heart beat. We assume the displacement between the slices of one heartbeat to be minimal and propagate the optimal transformation parameters found for the first slice as start parameters for its spatial successors

$$X_{ij}^{0} = X_{i-1j}^{\mathrm{opt}}, i > 1 \tag{7}$$

A detailed description of the algorithm is provided in the Appendix.

IV. IMAGE ANALYSIS

The image analysis required for a comprehensive cardiac perfusion analysis includes segmentation of the coronary arteries, segmentation and quantification of scarred tissue in the late enhancement images, detection of hypoperfused myocardial regions and finally a joint analysis. The image analysis methods that are applied to this end are described in this section.

A. Overview of Existing Approaches for Cardiac MR Image Analysis

1) Coronary Tree Analysis: Many methods for analyzing the course of the coronary arteries in MR images are based on a prefiltering to avoid artifacts and to enhance tubular structures [33]–[36]. While various approaches exist for the general vessel segmentation problem, e.g., region growing [37], wavefront propagation [38], Vessel Tracking [39] or model-based algorithms [40], only few methods deal specifically with the coronary arteries. These methods combine the segmentation with a centerline path determination [41], [42] or use an adapted region growing approach [43]. Although the feasibility of segmentation and even quantification of coronary arteries from MR angiographies has been shown in principle [44], algorithms dedicated for this task are missing.

2) Late Enhancement Detection: A common method for the detection of infarcted tissue in late enhancement images is the application of a threshold two or three standard deviations above the average intensity value of a healthy myocardial region [3]. An extension of this method, which applies a combination of both thresholds, is used to further classify infarctions into core and peri-infarct regions [5].

To support the late enhancement detection, there exist different approaches to compute a threshold automatically [25], [45], apply clustering approaches [46], or classify myocardial voxels based on support vector machines [47].

As the supplying arteries run inward from the outer myocardial surface (epicardium) to the inner surface (endocardium) and contraction may hinder the blood flow, in coronary artery disease infarctions grow from the inner to the outer part of the my-
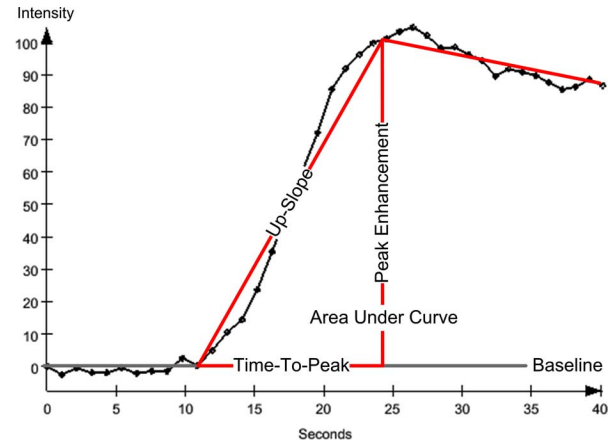

Fig. 6. Typical time-intensity-curve and its descriptive curve parameters.

ocardium [48]. This fact has been considered in the approach of Hsu *et al.* [49], who perform a feature analysis after the initial thresholding. In addition to checking the subendocardial distance, a 3-D connectivity analysis is applied to remove false-positive segmentations. Infarcted tissue does not necessarily appear as a homogeneous bright area in the late enhancement images; there are also dark regions, so-called no-reflow areas from microvascular obstructions, where no contrast agent can advect. The segmentation of these regions can either be derived from the intensity histogram [50], from the borders of segmented bright areas and the myocardial surface [49] or learned by a classifier [47]. For therapy decisions it is important to know the transmurality, i.e., the degree of penetration of myocardium with infarction from endocardium to the outer surface [51]. For this purpose, many approaches simply determine the portion of segmented voxels per radial segment [52], [53]. However, these methods do not consider the position of the segmented voxels relative to epi- and endocardium.

3) Perfusion Analysis: The inspection of the myocardial perfusion is based on the analysis of the time-intensity-curves of image regions or single voxels (cf. Fig. 6). Parameters computed from these curves are used to assess the local perfusion. These parameters can be so-called semi-quantitative descriptive curve parameters or quantitative parameters that describe a pharmacological process based on model assumptions about the imaged tissue compartments [54]. Descriptive parameters used for semi-quantitative analysis are peak enhancement (PE), up-slope, contrast agent arrival, time-to-peak (TTP), and area under curve (AUC) (Fig. 6) [55]–[57]. To reduce the influence of noise on the parameter calculation, many approaches fit model curves of pharmacokinetic processes like the so-called Gamma-variate before parameters are calculated from the given curves [58]–[60]. To assess the effect of a stenosis on the myocardial perfusion, sequences acquired at rest are compared with sequences acquired under pharmacologically induced stress [61]. The ratio of curve parameters derived for spatially corresponding regions from the different image sequences is used to assess the ability to increase perfusion under stress. Studies have shown that up-slope is the most appropriate parameter for this computation [55], and the myocardial perfusion reserve index (MPRI) has been proven suitable for locating

hypo-supplied myocardial regions [62]. As the resolution in myocardial perfusion images is very low and distortions from motion and acquisition artifacts are likely to be present, myocardial perfusion parameters are often calculated for image regions rather than for single voxels to achieve more stability through averaging [25], [63]. However, more accurate information about location, size and degree of a hypoperfusion are of clinical interest, and there are some approaches to segment suspicious regions based on the inspection of voxel intensity curves. These use different classification approaches like factor analysis, fuzzy K-means [64] and support vector machines [65], but they do not incorporate spatial constraints given for the location of infarctions relative to the myocardial surface (see Section IV-B-2).

B. Proposed Methods for the Combined Image Analysis and Inspection

1) Coronary Tree Analysis: For coronary artery segmentation we apply the region growing method as described by Boskamp *et al.* [43], [66]. The algorithm is originally designed for the segmentation of coronary arteries in computed tomography (CT) image volumes and thus does not take contrast inhomogeneities or signal dropout artifacts into account that occur in the presence of stents in MR angiographies. However, an interactive extension of the segmentation result is supported and we therefore use the algorithm to analyze the course of the coronary arteries.

2) Late Enhancement Analysis: In contrast to most approaches described in Section IV-A-2, we do not only want to measure the portion of infarcted tissue in a predefined tissue region, but also to locate the surface of the infarcted region. This information is used to visualize location, shape and transmurality of the infarction, and to compare it with the hypoperfused tissue regions derived from the perfusion images. To this end, we propose an algorithm that combines a histogram analysis with a constrained watershed segmentation [67]. The method is based on some fundamental properties of the processed images and the characteristics of myocardial infarctions.

- The intensity values of MR images are distributed according to the Rician distribution [68].
- Late enhancement is most likely to appear subendocardially.
- Relevant late enhancement regions are compact crescent-shaped areas of a certain size.
- Dark regions surrounded by late enhanced tissue are no-reflow-areas and thus belong to the infarct.

The first step in late enhancement detection is the segmentation of the myocardium. This is done semi-interactively with a Live-Wire-algorithm [69]. Segmentations can be interpolated between slices and optimized using a predefined cost function. Once the myocardium has been segmented, the intensity distribution is analyzed by fitting a mixture model of a Rayleigh distribution and a Gaussian distribution

$$h(x) = \underbrace{\alpha_R \frac{x}{\sigma_R} e^{-\frac{x^2}{2\sigma_R^2}}}_{\text{Rayleigh distribution}} + \underbrace{\alpha_G \frac{1}{\sqrt{2\pi}\sigma_G} e^{-\frac{1}{2}\left(\frac{x-\mu}{\sigma_G}\right)^2}}_{\text{Gaussian distribution}}. \quad (8)$$

These distributions are special cases of the Rician distribution, which are adequate for representing low and high intensities,

respectively. We assume that the Rayleigh distribution is suitable to represent the darker healthy myocardium, whereas the intensity distribution of the bright late enhanced regions can be described by the Gaussian distribution. The mixture model is fitted using the expectation maximization algorithm as described in the Appendix. Fig. 7 shows the example of a myocardial intensity distribution and the adapted mixture model. The thresholds t_M and t_D define the locations of the Rayleigh and the Gaussian distribution respectively, and t_S defines the intersection between these densities in the adapted model. Based on this mixture model, all myocardium voxels are assigned an estimated portion $p(x)$ of late enhanced tissue according to their intensity value x. We assume a linear partial volume model

$$p(x) = \begin{cases} 0, & \text{if } x \leq t_M \\ \frac{x - t_M}{t_D - t_M}, & \text{if } t_M < x \leq t_D \\ 1, & \text{if } t_D < x. \end{cases} \quad (9)$$

For the segmentation of late enhancement regions we apply a watershed segmentation, which uses the threshold t_D. According to the assumptions about the spatial features of myocardial infarctions, suitable basins have to be at least partially located in the subendocardial layer of the myocardium. Thus, we determine seed voxels v with a shorter distance d from the endocardial wall (endo) than from the epicardial wall (epi), and with an intensity value x higher than the determined threshold t_D

$$\left(\frac{d(v, \text{endo})}{d(\text{epi}, \text{endo})} \leq 0.5 \right) \wedge (p(x) = 1). \quad (10)$$

In the special case, where the intersection t_S of the Rayleigh and the Gaussian distribution is not located between the maxima t_M and t_D we apply $t_D = t_S$. The seed voxels v are used to define the basins included into the initial segmentation mask.

In an ensuing connected component analysis, small noisy structures are identified and removed from the segmentation result. To include the above-mentioned no-reflow-areas into the segmentation, holes are filled and the value of $p(x)$ is set to 1 for all voxels inside these holes. The resulting mask is used to visualize the extent of the infarcted tissue. To quantify the portion of infarction, the mask voxels, weighted with $p(x)$, are counted.

3) Detection of Hypoperfused Areas in Perfusion Images: The purpose of the perfusion analysis is to objectively determine hypoperfused tissue. As the range of intensity values and the point of intensity saturation vary with the particular acquisition settings of the individual examinations, it is difficult to define an objective measure for the degree of a hypoperfusion. Instead, we derive semi-quantitative parameters from the voxel-intensity-curves of the perfusion sequence (cf. Section IV-A-3) and provide a semi-automatic segmentation in the resulting parameter images.

The perfusion analysis starts with an interactive segmentation of the myocardium. Thanks to the initial motion correction step, only one segmentation has to be carried out per slice. Before computation of the up-slope parameter, the voxel intensity curves $x(t)$ are corrected by their baseline value in the reference time frame $x(t_M)$

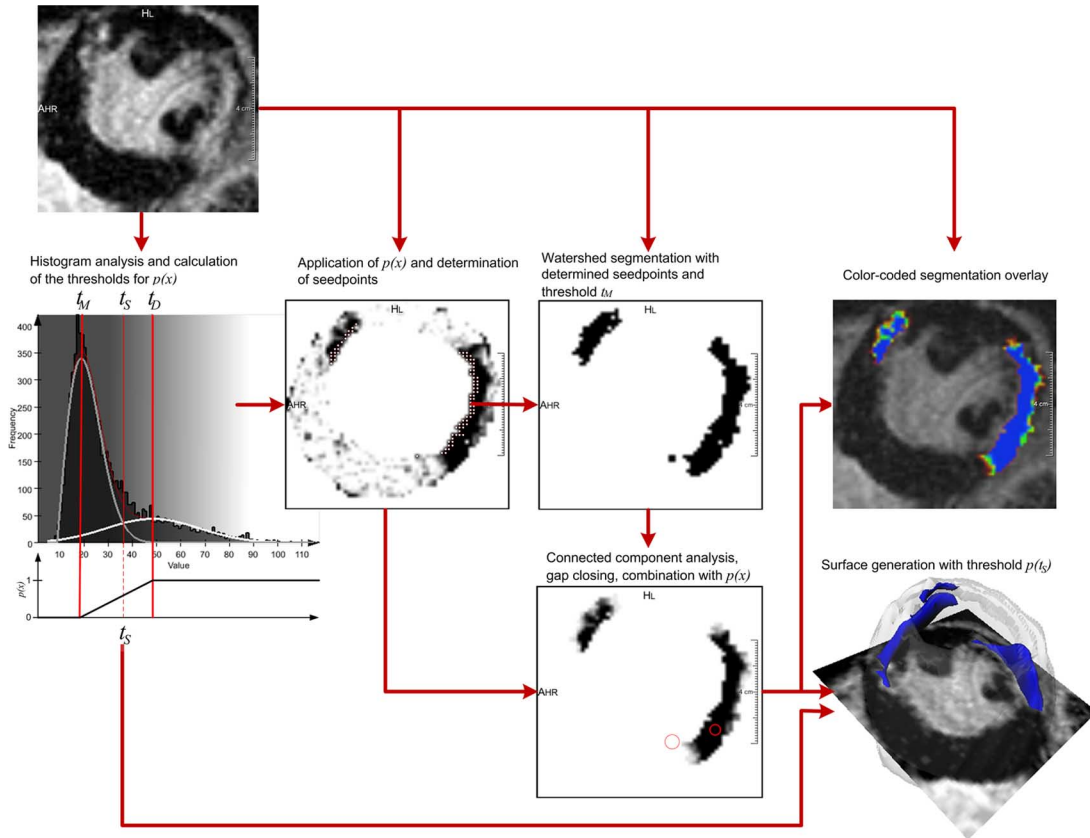$$\tilde{x}(t) = \frac{x(t) - x(t_M)}{x(t_M)}. \quad (11)$$

Fig. 7. Late enhancement segmentation procedure. The thresholds t_M, t_D, and t_S that are derived from the initial histogram analysis are used to control the watershed segmentation and to determine a function for the potential portion of hyperenhanced tissue $p(x)$ for an intensity value x. This function is applied for the detection of the initial seed voxels v (white markers) as well as for the final quantification. t_S defines the threshold for the 3-D surface generation. The red circles show locations where the original watershed segmentation was changed by the subsequent connected component analysis and the closing of gaps.

This baseline correction serves as an inhomogeneity correction when the corrected displacement within the perfusion sequence is relatively small. However, especially for the application to data acquired with higher field strengths, an inhomogeneity correction should be performed prior to motion correction.

As shown in Fig. 2, perfusion images acquired at rest and under stress do not show the myocardium in the same heart phase. Therefore, a voxel-wise computation of the MPRI (cf. Section IV-A-3) is impossible for most images. We propose a segmentation method for the stress perfusion sequence and a subsequent region-based calculation of the myocardial perfusion reserve to control the result. To segment the hypoperfused regions, the user has to define a segmentation threshold in the histogram of the computed slope parameter image. The resulting mask is filtered by applying a connected component analysis, which removes clusters with a border length of less than eight voxels. An example is shown in Fig. 8.

4) Combined Inspection of Results: The combined inspection of the information extracted in the analysis steps aims at clarifying the relation between structures that differ in coverage and information density. To give an impression of the spatial relations of infarction and hypoperfusion by means of a 3-D visualization, image data and segmentation results are shown in different combinations. Vessels and segmented infarction, which are segmented in datasets with relatively dense information are
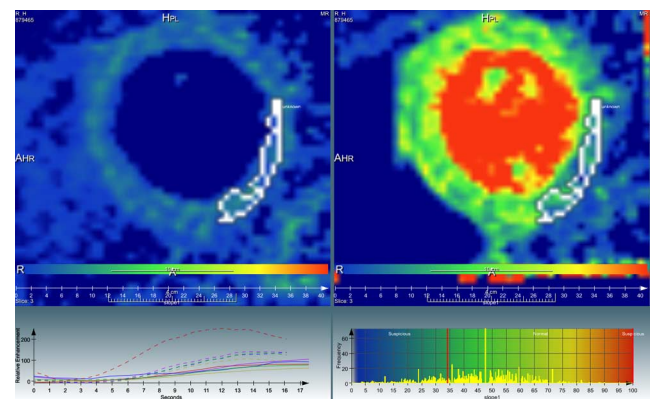

Fig. 8. Segmentation of perfusion parameter images. The images in the upper row show the up-slope parameter for rest and stress perfusion. The contours correspond to the threshold marked in the stress parameter histogram in the lower diagram. The curves in the diagram on the left represent the intensity courses in the contoured regions (solid: rest, dashed: stress).

shown as 3-D surface renderings. In contrast, perfusion information is very sparse. To make this clear, the contours of the segmented hypoperfused regions are shown at the locations of the corresponding image slices. Further information about the relation to the left ventricular wall is depicted by an additional transparent surface rendering of the myocardium segmentation

TABLE III
DATASETS FOR EVALUATION

| #	O	Whole-heart Res.(mm,mm,mm)	Ext.(x,y,z)	Q	Late Enhancement Res.(mm,mm,mm)	Ext.(x,y,z)	Q	Perfusion Res.(mm,mm,mm)	Ext.(x,y,z,t)	Stress	Rest
1	Axial	(0.63, 0.63, 1.1)	(512, 400, 120)	1	(1.33, 1.33, 10.0)	(208, 256, 5)	2	(1.67, 1.67, 18.4)	(160, 192, 3, 40)	2	2
2	Axial	(0.50, 0.50, 1.5)	(640, 480, 60)	3	(1.25, 1.25, 10.0)	(208, 256, 6)	2	(1.68, 1.68, 12.0)	(160, 192, 3, 40)	3	2
3	Axial	(0.78, 0.78, 1.1)	(512, 368, 104)	2	(1.33, 1.33, 10.0)	(208, 256, 7)	1	(1.98, 1.98, 16.0)	(160, 192, 3, 40)	2	2
4	Sagittal	(1.54, 1.54, 1.5)	(128, 128, 120)	2	(1.33, 1.33, 10.0)	(208, 256, 8)	1	(1.88, 1.88, 12.0)	(192, 144, 3, 40)	2	2
5	Axial	(0.64, 0.64, 1.2)	(512, 368, 112)	2	(1.33, 1.33, 10.0)	(208, 256, 7)	2	(1.88, 1.88, 16.0)	(160, 192, 3, 40)	3	2
6	Axial	(0.63, 0.63, 1.2)	(512, 368, 112)	1	(1.33, 1.33, 10.0)	(208, 256, 8)	1	(1.67, 1.67, 16.0)	(160, 192, 3, 40)	2	3
7	Axial	(0.63, 0.63, 1.3)	(512, 368, 72)	2	(1.25, 1.25, 10.0)	(208, 256, 7)	1	(1.82, 1.82, 14.4)	(160, 192, 3, 40)	2	2
8	Axial	(0.63, 0.63, 1.8)	(512, 368, 72)	2	(1.33, 1.33, 10.0)	(208, 256, 8)	2	(1.67, 1.67, 16.0)	(160, 192, 3, 40)	3	3
9	Axial	(0.63, 0.63, 1.2)	(512, 368, 120)	3	(1.33, 1.33, 10.0)	(208, 256, 7)	2	(1.98, 1.98, 16.0)	(160, 192, 3, 40)	3	3
10	Axial	(0.63, 0.63, 1.8)	(512, 368, 52)	3	(1.33, 1.33, 10.0)	(208, 256, 7)	2	(1.82, 1.82, 16.0)	(160, 192, 3, 40)	3	3
11	Sagittal	(1.54, 1.54, 1.5)	(128, 128, 104)	3	(1.33, 1.33, 10.0)	(208, 256, 7)	2	(1.56, 1.56, 12.0)	(160, 192, 3, 40)	3	3
12	Axial	(0.63, 0.63, 2.0)	(512, 368, 57)	2	(1.33, 1.33, 10.0)	(208, 256, 8)	2	(1.98, 1.98, 16.0)	(160, 192, 3, 40)	2	2
13	Axial	(0.55, 0.55, 1.5)	(640, 480, 80)	1	(1.41, 1.41, 10.0)	(256, 200, 8)	1	(2.08, 2.08, 16.0)	(160, 192, 3, 40)	2	2
14	Axial	(0.53, 0.53, 1.5)	(640, 480, 80)	2	(1.33, 1.33, 10.0)	(208, 256, 9)	1	(1.88, 1.88, 14.4)	(144, 192, 4, 40)	2	2
15	Axial	(0.50, 0.50, 1.5)	(640, 480, 72)	2	(1.33, 1.33, 10.0)	(208, 256, 9)	2	(2.08, 2.08, 16.0)	(160, 192, 3, 40)	2	2
16	Axial	(0.50, 0.50, 1.5)	(640, 480, 80)	2	(1.33, 1.33, 10.0)	(208, 256, 11)	2	(1.98, 1.98, 16.0)	(160, 192, 3, 40)	2	2
17	Axial	(0.63, 0.63, 1.1)	(512, 368, 128)	2	(1.33, 1.33, 10.0)	(224, 256, 7)	2	(1.98, 1.98, 16.0)	(160, 192, 3, 40)	2	2
18	Axial	(0.63, 0.63, 1.1)	(512, 368, 120)	2	(1.37, 1.37, 10.0)	(224, 256, 10)	2	(1.98, 1.98, 24.0)	(160, 192, 3, 40)	2	2
19	Axial	(0.66, 0.66, 1.3)	(512, 368, 80)	2	(1.33, 1.33, 10.0)	(224, 256, 7)	2	(1.98, 1.98, 16.0)	(160, 192, 3, 40)	2	2
20	Axial	(0.63, 0.63, 1.2)	(512, 368, 96)	2	(1.33, 1.33, 10.0)	(208, 256, 7)	2	(1.98, 1.98, 16.0)	(160, 192, 3, 40)	2	2
21	Axial	(0.66, 0.63, 1.1)	(512, 368, 112)	2	(1.25, 1.25, 10.0)	(200, 256, 10)	2	(1.67, 1.67, 12.0)	(150, 192, 3, 40)	2	2
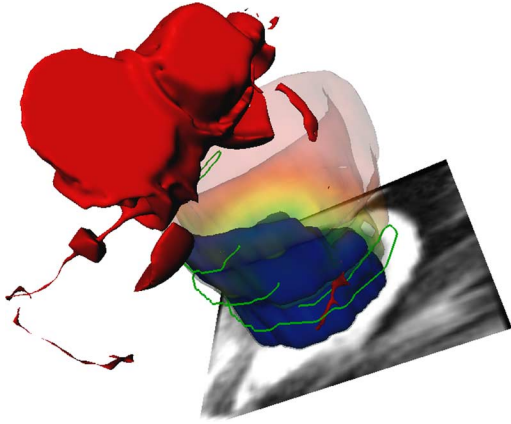
Fig. 9. Combined visualization of the segmentation results. The segmented infarction is shown as a dark blue surface, whereas the hypoperfused regions are represented by contours that are located in the corresponding perfusion image slices. The myocardium, which is segmented in the late enhancement images, is shown as a transparent surface. The color of the surface depends on the distance to the infarction surface.

from the late enhancement dataset. Fig. 9 shows an example of such a combination.

V. RESULTS

The methods described in the previous sections were integrated in a software application and applied to 21 cardiac MRI datasets of patients with suspected CAD from clinical routine. Image data were acquired with different scanners and vary in orientation (O), resolution (Res.), extent (Ext.), and quality (Q). Image quality was assessed by a radiologist on a scale from 1 for good, over 2 for medium to 3 for poor image quality. Table III shows the resolution in z-direction as a combination of slice thickness and slice distance to give a comprehensive impression of the image space represented by one slice. The real slice thickness is 5 mm for the late enhancement image and around 8 mm for the perfusion image sequences. Image analysis steps as well as the assessment of results were performed by two radiologists.

A. Image Alignment

To assess the quality of the preprocessing results and to allow further processing in case of failure, manual correction methods were provided for all alignment steps.

1) Alignment of Late Enhancement Images: Late enhancement images were aligned slice-wise with the corresponding whole-heart volume as described in Section III with NMI and NCC as similarity measures. Transformation parameters were saved for each slice. The transformed images were checked by the experts in a 3-D view and in a 2-D overlay view, which show a combination of the transformed slice and the corresponding reference whole-heart volume. Fig. 10 shows the example of a successfully aligned late enhancement slice. Overall, 168 slices had to be inspected. The experts had to either accept or manually correct the alignment result. Table IV shows the assessment results. In Fig. 11, translation and rotation parameters are plotted together for each slice. The translation parameter values are expressed relative to the size of the transformed image. Values outside the interval $[-1, 1]$ indicate that the image is moved completely out of its original bounding box. The rotation is given in radian measure. The parameter correlation is 0.3 for all slices and 0.4 if only those slices are considered for which both observers accepted both methods. For these cases the correlation values of the translation in x- and y-direction, respectively, are 0.64 and 0.85 whereas for rotation the correlation value is 0.24.

2) Alignment of Perfusion Images: The first step in the preprocessing of perfusion images was an interactive cropping with removal of heavily distorted image time frames. In this step, up to 14 time frames were removed from the inspected sequences. The resulting time series were processed as described in Section III-B-2.

First, the reference image in the perfusion sequence was aligned with the whole-heart image. For this alignment, NMI and NCC were applied as similarity measures analogous to the alignment of the late enhancement images. The registration of whole-heart image and the perfusion reference image was
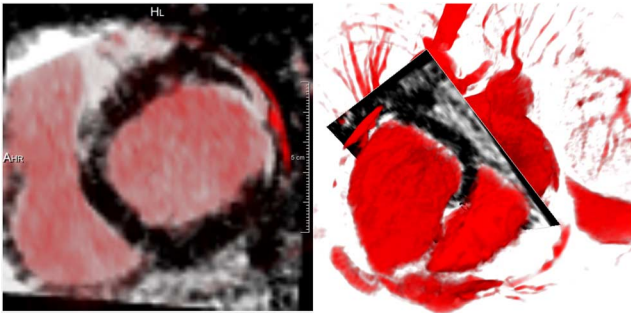
Fig. 10. Control views for interactive alignment assessment. The late enhancement image slice in the left viewer corresponds to the slice shown in 3-D. The whole-heart image is displayed as a red overlay in the 2-D image and by volume rendering in 3-D.

TABLE IV
NUMBER OF LATE ENHANCEMENT SLICES ACCEPTABLY ALIGNED WITH THE WHOLE-HEART IMAGE USING NMI AND NCC

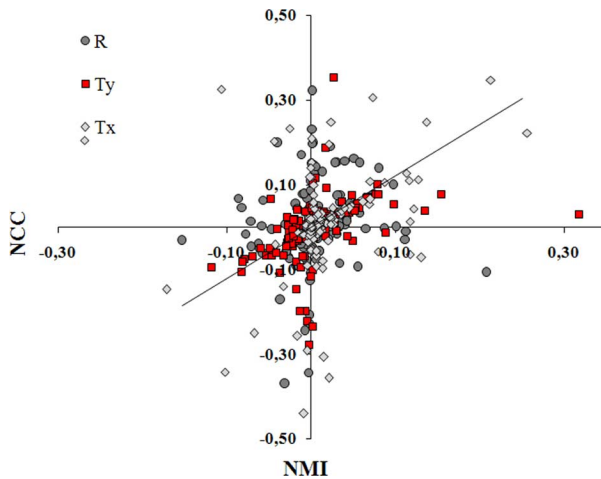|	NMI		NCC	
Observer 1	142	84%	131	87%
Observer 2	150	89%	141	94%
Agreement	139	93%	125	83%

Fig. 11. Comparison of translation and rotation for slice alignment correction with NMI and NCC. Translation values *Tx* and *Ty* are given relative to the image size and can take values between -1 and 1, while the rotation *R* is shown in radian measure.

TABLE V
NUMBER OF PERFUSION SLICES ACCEPTABLY ALIGNED WITH THE WHOLE-HEART IMAGE USING NMI AND NCC

	NMI		NCC	
Observer 1	116	91%	116	91%
Observer 2	109	85%	113	88%
Agreement	102	80%	104	81%

assessed by the experts as described in Section V-A-1. The results are shown in Table V. Both experts accepted 102 slices aligned with NMI and 104 slices aligned with NCC. However, the accepted slice sets do not fully overlap: 93 slices were acceptably registered with both measures, and for 20 slices the observers approved the result of one measure.
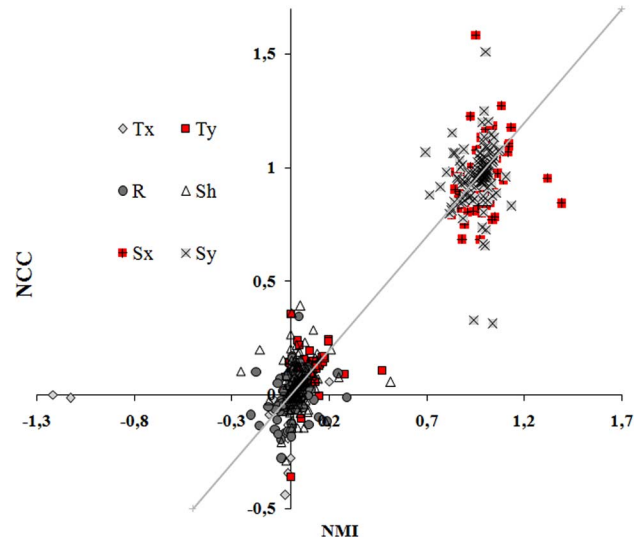

Fig. 12. Comparison of transformation parameters for the alignment of perfusion slices with the corresponding whole-heart volume using NMI and NCC. *Tx* and *Ty*, respectively, represent the translation given relative to the image size $[-1, 1]$, the rotation *R* is expressed in radian measure, *Sh* represents the shearing and *Sx* and *Sy*, respectively, represent the applied scaling.
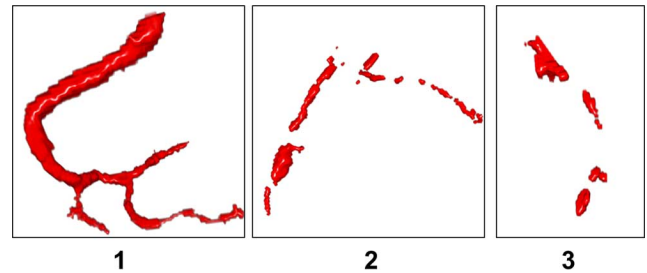

Fig. 13. Examples for vessel segmentations assessed with scores from 1 for good quality to 3 for poor quality. A score of 4 indicates that the branch of interest has not been segmented.

Fig. 12 shows the values of the affine transformation parameters considered as optimal by NCC plotted against the corresponding values computed with NMI. For a comprehensive overview, all values are plotted in one diagram. Translation and rotation are expressed, as described in Section V-A-1. The outliers of the translation and scaling values belong to transformations not accepted by the observers. The correlation of the parameters determined with NCC and with NMI is 0.96. The subsequent motion correction was considered as successful for the relevant part of the time series by both experts in all cases.

B. Image Analysis

1) Coronary Tree Segmentation: The coronary arteries were segmented interactively with the method described in Section IV-B-1 by both experts. The segmentation of the main branches, the right coronary artery (RCA), the left coronary artery (LCA), and the left circumflex (LCX) was then assessed with scores from 1 to 4 as shown in Fig. 13:

- 1) Proper segmentation including the distal parts of the branch.
- 2) Small gaps in the vessel course.

TABLE VI
QUALITY ASSESSMENT OF THE SEGMENTED CORONARY BRANCHES

Quality	LCX				LAD				RCA			
	1	2	3	4	1	2	3	4	1	2	3	4
Observer 1	4	8	7	2	3	11	6	1	7	8	4	2
Observer 2	1	8	11	1	1	8	11	1	7	5	6	3
Agreement	1	8	7	1	1	8	6	1	7	5	4	2

TABLE VII
CORRELATION OF LATE ENHANCEMENT SEGMENTATION RESULTS

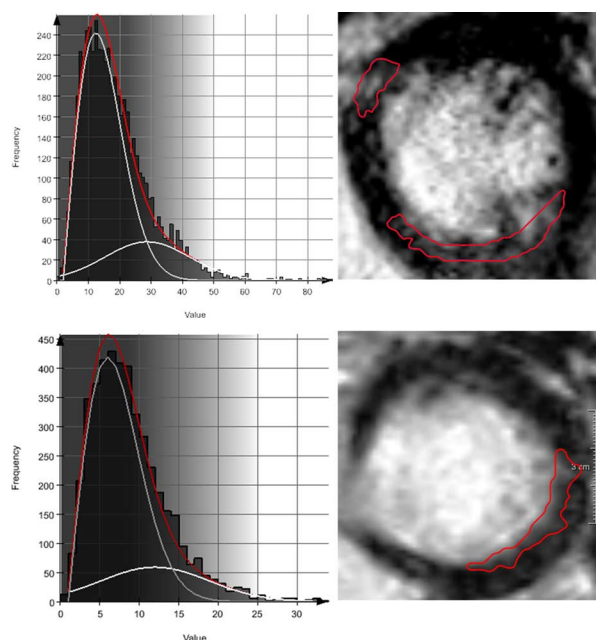| Observer	Observer	Manual		3σ-Method	
		1	2	1	2
Automatic		0.95	0.94	0.69	0.78
Manual	1		0.93	0.70	0.80
	2			0.67	0.76
3σ-Method	1				0.89

Fig. 14. False positive late enhancement segmentation for patient 9 (upper row) and 10 (lower row). The results of the histogram analyses are shown on the left, whereas the corresponding segmentation results are represented by the gray contours in the images on the right.

- 3) Partial segmentation. The vessel course can still be estimated.
- 4) The branch of interest is not detectable.

In all but one of the 21 datasets, it was possible to segment coronary arteries. Table VI shows the assessment of the segmented left circumflex (LCX), left anterior descending (LAD), and right coronary artery (RCA) for both observers. The experts agreed in their grading for 51 of 60 segmented branches (85%). Acceptable segmentations (score 1 or 2) were achieved by both observers for the LCX and the LCA in 43% of all cases, whereas the RCA could be segmented acceptably in 57% of all cases. In 33% the RCA segmentation was rated with 1 by both observers. The segmentation of the LCX and the LCA, respectively, achieved good results in only 5% percent of all cases.
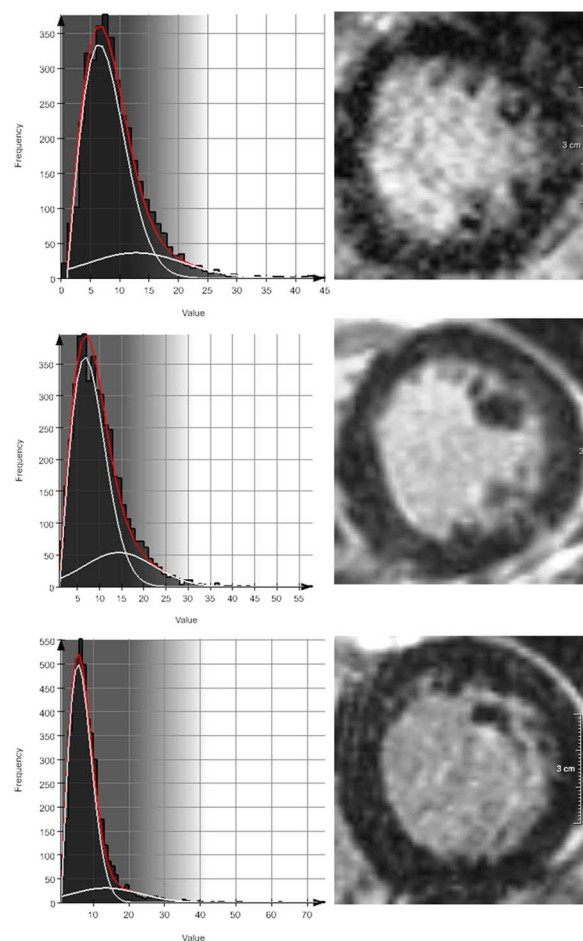

Fig. 15. Correct results for patient 3, 8, and 17. No late enhancement regions are detected by the automatic histogram-based method.

2) Late Enhancement Detection: The late enhancement segmentation was performed automatically with the methods described in Section IV-B-2. The experts were then allowed to change the segmentation manually. Furthermore, the experts drew regions into myocardial tissue that they assumed to be healthy. These were analyzed to determine a threshold three standard deviations (3σ) above the average. Fig. 16 shows the comparison of the determined late enhancement volume portions per AHA-segment with all performed segmentations using Bland–Altman and scatter plots. The correlation between the manual and the automatic segmentations proposed here was better than between the manual and the 3σ-method segmentation. Furthermore, the 95% confidence interval is significantly smaller for the comparison of automatic and manual segmentations than for the interobserver comparison of the 3σ-method. The correlation between the applied segmentations is shown in Table VII.

The observers agreed on the nonexistence of late enhancement in five cases. As shown in Fig. 14, the automatic segmentation method detected false-positive late enhancement regions in two of these cases. For the other three cases the automatic segmentation agreed with the observers' segmentations (Fig. 15). For cases 5, 6, 7, and 16, observer 1 determined bright regions, which could possibly represent late enhancement. These regions
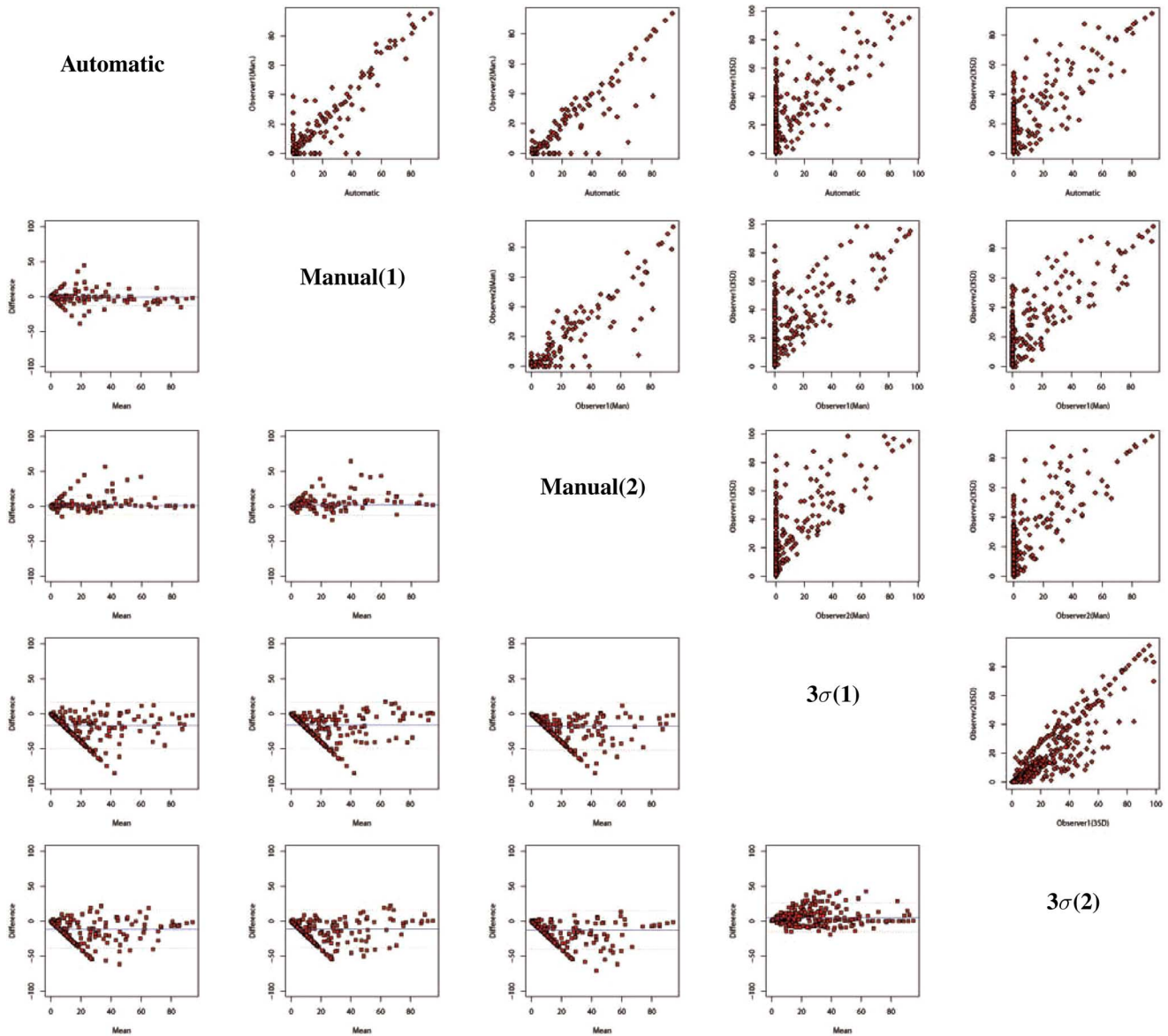
Fig. 16. Comparison of the portion of segmented tissue per AHA segment for automatic and expert segmentation. The upper triangular matrix shows scatter plots corresponding to the results achieved with the methods stated in the corresponding diagonal elements. The opposite elements in the lower triangular matrix show these results in Bland–Altman plots. (1) and (2), respectively, indicate which expert did the segmentation.

were neither detected by the automatic method nor considered relevant by observer 2.

3) Perfusion Analysis and Combination of Results: The methods were applied to clinical routine datasets of human subjects. Thus, no histopathological findings were available and the results could only be assessed using the findings from other clinical examinations like for example conventional catheter angiography, if available. Based on this information, the experts decided whether the visualized results were plausible and could provide relevant information about the relations of the relevant structures determined in the different datasets. All available results were processed in this combination step. Visualizations are shown in Fig. 17. For those cases where the observers agreed on the existence of a relevant infarction or hypoperfusion, the observers had to determine how accurate the supplying artery could be identified. The expert graded this assignment

with 2 when the identification of the supplying artery was considered certain and 1 if it could be estimated. 0 means that the visualization provided no helpful information regarding the relation between infarctions and supplying arteries (Fig. 18).

The presented relations were considered plausible in all inspected cases. Table VIII shows the assessment results.

VI. DISCUSSION

A. Slice Alignment and Motion Correction

The results of the registration assessment show that the alignment of late enhancement images with the whole-heart volume was slightly more successful with NMI as similarity measure than with NCC. The agreement concerning the misaligned slices was marginal for both late enhancement and perfusion images.
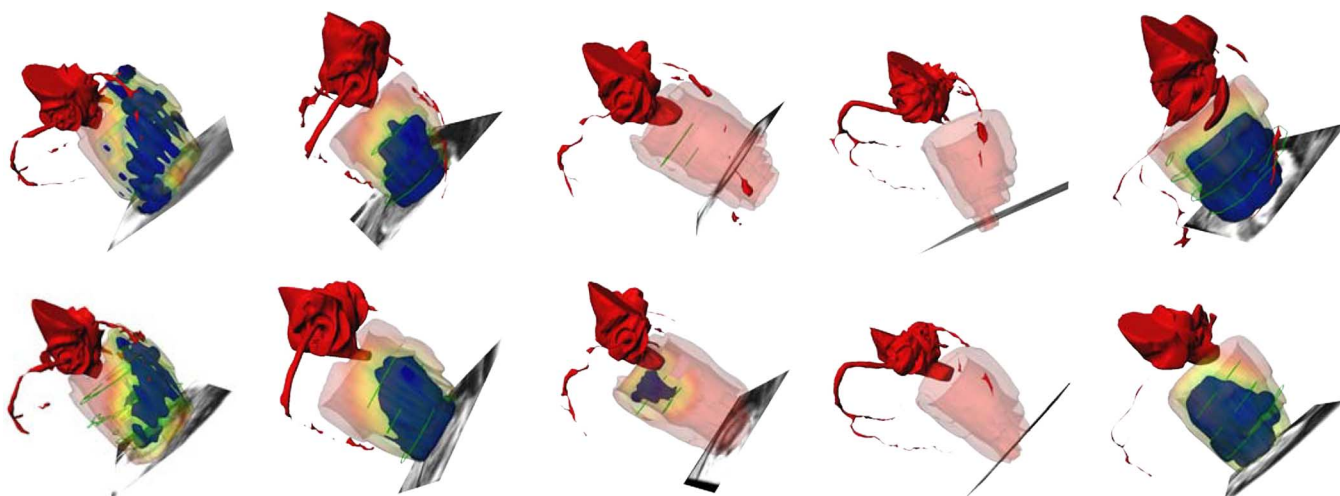
Fig. 17. Visualization of the combined analysis results for cases 1, 15, 5, 6, and 14. The rows show the results of observer 1 and observer 2, respectively.
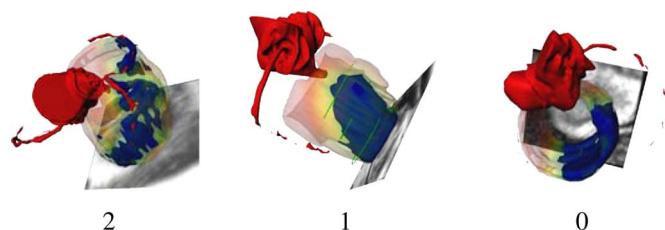
Fig. 18. Assessment of the correlation between hypoperfusion/infarction and the supplying artery. 2: clear correlation of the infarcted tissue regions with the LAD, 1: The correlation between the infarcted region and the RCA can be estimated. 0: There is no clear correlation of the infarcted region with a coronary branch.
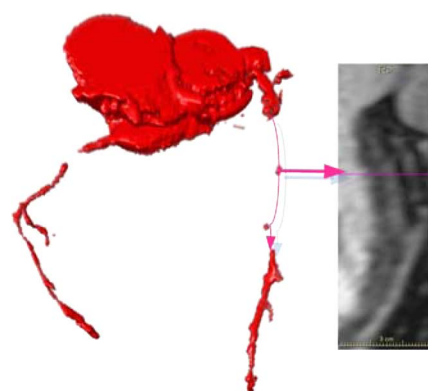
Fig. 19. Tree segmentation with interruption due to signal drop-out caused by a stent. The image on the right shows the curved MPR of the path through the vessel and clearly depicts the interruption of the bright vessel course near the stent.

TABLE VIII
ASSESSMENT OF THE ASSIGNMENT

#	LCX 1	LCX 2	LAD 1	LAD 2	RCA 1	RCA 2
1			2	2		
2	2	2				
4	1	2	1	2		
11	1	1				
12			2	2		
13	2	1				
14			2	2		
15			2	2	1	1
18	1	1	1	1		
19	1	2	2	2		
20					2	2

beneficial to include translation along the long-axis as proposed by Lötjönen *et al.* [13] and Barajas *et al.* [14].

The motion correction was accepted in all cases and thus considered successful. However, due to the floating reference image, the method heavily depends on the removal of outliers with strong out-of-plane motion. The observers removed up to 14 time frames from the perfusion sequences before the motion correction started and thus decreased the temporal information density considerably. In addition to the automatization of this step, its influence on the reliability of derived results has to be addressed in further research.

B. Image Analysis

A satisfactory vessel segmentation (category 1 or 2) was assigned by both experts to only 25 of 63 relevant coronary branches. The region growing approach adopted here was mainly hampered by stenoses and stents (Fig. 19), or it leaked into adjacent structures. Tracking approaches, which can bridge gaps and control the shape of the segmented structure might be more successful here.

The results of the late enhancement analysis appear very promising. The automatically segmented late enhancement

Furthermore, for many misaligned slices the transformation parameters show implausible values. This indicates that it could be beneficial to restrict the parameter range by a reformulation of the optimization function to introduce constraints in the optimization.

For both late enhancement and perfusion slice registration, we did not allow translation in the long-axis direction, although this is likely to occur. For the late enhancement image, we wanted to preserve the volumetric information which would be changed by the interpolations resulting from a slice position change. However, to provide correct information, it could be
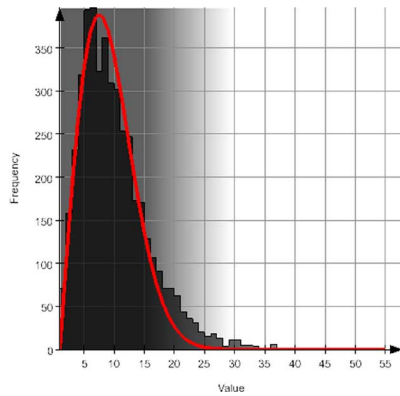
Fig. 20. Histogram and fitted Rayleigh distribution (red curve) for patient 8. Although there is no late enhancement, the red curve does not perfectly match the histogram. This might be due to partial volume effects at the myocardial borders.
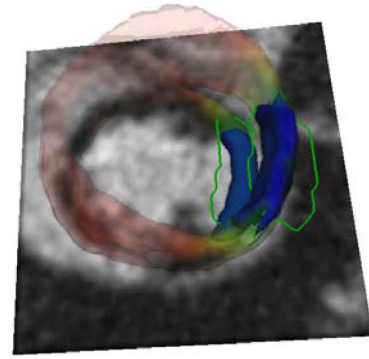

Fig. 21. Misalignment between segmented hypoperfusion and infarction due to the difference in wall thickness (case 12). The segmentation of the hypoperfusion partly overlaps with the blood pool of the late enhancement image.
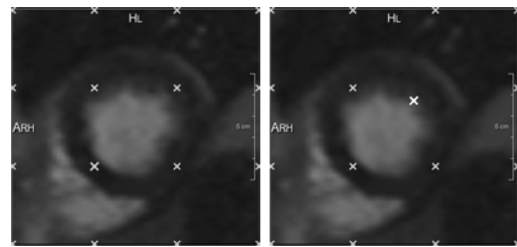

Fig. 22. *B*-Spline transformation: The white crosses in the image define the positions of the control points. The right image is transformed according to the translation of the bold cross from its position in the left image.

regions show a good correlation with the manual expert segmentations, whereas the 3σ-method does not. Fig. 16 shows clearly that for many segments the volumes resulting from the 3σ-thresholding are remarkably higher than those determined manually and with the mixture model. The largest differences between the methods occurred in the apical segments, where the image quality often is low due to motion artifacts. To achieve better results for this part of the myocardium, it might be beneficial to include long-axis slices into the analysis. The method delivered false-positive results for two cases. In further research the application of information criteria like Akaikes Information Criterion [70] or the Bayesian Information Criterion [71] could be applied to decide whether a single Rayleigh distribution or a mixture model are more appropriate for the description of the given histogram. As shown in Fig. 20 for patient 8 the Rayleigh distribution does not fit perfectly for all cases without late enhancement. Further studies will have to investigate whether this mismatch is based on partial volume effects at the myocardial borders and if better results can be achieved by fitting a Rician distribution as proposed recently by Friman *et al.* [72].

Regarding the perfusion analysis, the weakness of the proposed method could be the influence of the interactive segmentation, which was not assessed in the evaluation. Due to the sparseness, the low resolution, the motion artifacts, and the high number of processing steps that are necessary to derive processing results, perfusion analysis is likely to be error prone. However, both experts considered the results as reasonable in all cases. In addition to the interactive preprocessing steps, the result depends on the threshold setting for the segmentation. A reproducible automatic method based on standard values for the MPRI (cf. Section IV-A-3) could be developed, if a registration of stress and rest perfusion sequence were possible. For the image data inspected here, this was not considered reasonable due to the differences in the heart phases shown in stress and rest images (Fig. 2).

The combination of the results showed plausible results for most datasets, although the visualized information did not provide therapy relevant information in all cases. Fig. 21 shows an example where the hypoperfusion is located in the blood pool

of the late enhancement image. This occurs in cases where the myocardium is much thicker in the perfusion image than in the late enhancement image due to a contraction phase mismatch (Fig. 2). The accuracy in the association of defects and supplying artery strongly depends on the coverage of the coronary tree segmentation. In those cases where only short parts of the relevant branches could be segmented, a clear identification of the responsible coronary branch was impossible.

C. General Considerations

Major restrictions arise from the data characteristics caused by the acquisition technique such as a signal drop-out in the whole-heart image and the contraction phase mismatch in the perfusion sequences. While the first issue has to be addressed by advanced image processing methods such as for example vessel tracking approaches, the second problem requires a change in the sequence timing of the image acquisition protocols.

The proposed workflow still contains a considerable amount of interactive processing steps, especially in the analysis of perfusion and coronary arteries. The presented results show a good agreement in the experts' assessment of the coronary tree segmentations, but the current studies did not analyze the interobserver variability caused by the interactive preprocessing steps in the perfusion analysis. Further work should focus on the complete automatization of preprocessing by automatic detection of the region of interest and the removal of outliers from the perfusion sequences. To achieve a higher reproducibility in the perfusion and late enhancement analyses, an automatic myocardium segmentation, as proposed in several publications [73]–[75] would be helpful. Finally, larger clinical studies are

Find reference time frame $I_{P_{it_M}}$ in perfusion image I_P

$$t_M = \lfloor \tilde{t}_M \rfloor_{\text{Index}}, \; x_{\text{LV}}(\tilde{t}_M) = x_{\text{RV}}(\tilde{t}_M)$$

Align reference time frame $I_{P_{it_M}}$ with whole-heart image I_{WH}
$\forall I_{P_{it_M}}, i \in \{1, ..., z_{max}\}$

   1) **Initialization of parameters $X_{it_M}^0$**

$$X_{it_M}^0 = \begin{cases} id & , i = 1 \\ X_{i-1 t_M}^{opt} & , i > 1 \end{cases}$$

   2) **Repeat until convergence**

      a) Determine overlapping image regions for the current transformation parameters X_i^j

$$\begin{aligned} I_{P_{it_M}}^t &= T\left(I_{P_{it_M}}, X_{it_M}^j\right) \\ I_{P_{it_M}}^{t'} &= I_{P_{it_M}}^t |_{D_{P_i}^t \cap D_{\text{WH}}} \\ I_{\text{WH}}' &= I_{\text{WH}}|_{D_{P_i}^t \cap D_{\text{WH}}} \end{aligned}$$

      b) Calculate new parameters $X_{it_M}^{j+1}$

$$X_{it_M}^{j+1} = O_{\text{Simplex}}\left(X_{it_M}^j, S\left(I_{P_{it_M}}^{t'}, I_{\text{WH}}'\right)\right)$$

Fig. 23. Procedure for the alignment of the perfusion sequence reference time frame with the whole-heart image. S refers to the applied similarity measure, which is either NCC or NMI.

necessary to assess the reliability and reproducibility of the suggested methods.

The presented study focusses on the examination of the tissue perfusion state regardless of the effect on the tissue function. This might be a beneficial extension and should be the subject of further research.

VII. Conclusion

We present a comprehensive approach to computer aided cardiac perfusion analysis that allows a combined analysis of coronary arteries, myocardial perfusion, and late enhancement based on MR image data. For this purpose, we integrated existing and novel methods for alignment and combined analysis of the different types of images in one software. Experiments performed with this software demonstrate the successful applicability of the presented methods to clinical data and show the potential of the combined analysis in providing additional information on the spatial relation of infarction, hypoperfusion, and supplying vessels.

Appendix

A. Alignment of Perfusion Sequences

This section gives a brief overview over the algorithms applied for the registration of the perfusion sequences. The algorithm applied for the alignment of the perfusion sequences with the whole-heart volume is shown in Fig. 23, whereas the motion correction procedure is shown in Fig. 24.

1) Measuring Similarity With Normalized Cross Correlation and Normalized Mutual Information: To find the transformation parameters X for an optimal alignment of an image I_F with a reference image I_R we apply a similarity measure that

Motion Correction with affine and B-Spline transformations,
$X = \{XA, XB\}$
$\forall t \in \{t_M + 1, ..., t_{max}\}$
$\forall i \in \{1, ..., z_{max}\}$

   1) **Initialization of parameters $X_{it_M}^0$**

$$X_{it}^0 = \begin{cases} id & , i = 1 \\ X_{i-1 t}^{opt} & , i > 1 \end{cases}$$

   2) **Find transformation parameters for correction**

      a) **Optimize affine transformation parameters XA**
Repeat until convergence

        i) Determine overlapping image regions for current transformation parameters XA_i^j

$$\begin{aligned} I_{P_{it}}^t &= T\left(I_{P_{it}}, XA_{it}^j\right) \\ I_{P_{it}}^{t'} &= I_{P_{it}}^t|_{D_{P_{it}}^t \cap D_{P_{it-1}}^{t_{opt}}} \\ I_{P_{it-1}}^{t_{opt}'} &= I_{P_{it-1}}^{t_{opt}}|_{D_{P_{it}}^t \cap D_{P_{it-1}}^{t_{opt}}} \end{aligned}$$

        ii) Calculate new parameters XA_{it}^{j+1}

$$XA_{it}^{j+1} = O_{\text{Simplex}}\left(XA_{it}^j, S\left(I_{P_{it}}^{t'}, I_{P_{it-1}}^{t_{opt}'}\right)\right)$$

      b) **Optimize B-Spline transformation parameters XB**
Repeat until convergence

        i) Determine overlapping image regions for current transformation parameters $X_{it}^k = \{XA_{it}^{opt}, XB_{it}^k\}$

$$\begin{aligned} I_{P_{it}}^t &= T\left(I_{P_{it}}, X_{it}^k\right) \\ I_{P_{it}}^{t'} &= I_{P_{it}}^t|_{D_{P_{it}}^t \cap D_{P_{it-1}}^{t_{opt}}} \\ I_{P_{it-1}}^{t_{opt}'} &= I_{P_{it-1}}^{t_{opt}}|_{D_{P_{it}}^t \cap D_{P_{it-1}}^{t_{opt}}} \end{aligned}$$

        ii) Calculate new parameters XB_{it}^{k+1}

$$XB_{it}^{k+1} = O_{\text{Simplex}}\left(XB_{it}^k, S\left(I_{P_{it}}^{t'}, I_{P_{it-1}}^{t_{opt}'}\right)\right)$$

Fig. 24. Procedure for the alignment and motion correction of perfusion sequences. S refers to the applied similarity measure, which is either NCC or NMI.

has to be maximized. The image region that is considered for this measurement is defined as the intersection of the image domains D_R, D_F.

a) Normalized Cross Correlation: The cross correlation or covariance $\text{Cov}(I_R, I_F)$ of two images I_R and I_F is defined as shown in (13) and can be used as a measure for the similarity of the images

$$\begin{aligned} \text{Cov}(I_R, I_F) &= \frac{\sum_{(i,j)}\left(I_R'(i,j) - \overline{I_R'}\right)\left(I_F'(i,j) - \overline{I_F'}\right)}{|D_R \cap D_F| - 1} \\ \overline{I_R'} &= \frac{\sum_{(i,j)} I_R'(i,j)}{|D_R \cap D_F|} \\ \overline{I_F'} &= \frac{\sum_{(i,j)} I_F'(i,j)}{|D_R \cap D_F|} \\ I_R' &= I_R|_{D_R \cap D_F} \\ I_F' &= I_F|_{D_R \cap D_F} \end{aligned} \qquad (12)$$

By the normalization with $\mathrm{Var}(I_R)$ and $\mathrm{Var}(I_F)$ the measure becomes invariant against changes in scale and offset

$$\mathrm{NCC}(I_R, I_F) = \frac{\mathrm{Cov}(I_R, I_F)^2}{\mathrm{Var}(I_R')\mathrm{Var}(I_F')}$$

with

$$\mathrm{Var}(I_R') = \frac{\sum_{(i,j)}\left(I_R'(i,j) - \overline{I_R'}\right)^2}{D_R \cap D_F - 1}$$
$$\mathrm{Var}(I_F') = \frac{\sum_{(i,j)}\left(I_F'(i,j) - \overline{I_F'}\right)^2}{|D_R \cap D_F| - 1}. \tag{13}$$

b) Normalized Mutual Information: Normalized mutual information is based on the Shannon entropy [76], which measures the uncertainty in a set of events regarding the deducable amount of information. In the application to images I the events are the intensity values $x \in R(I)$, which occur with frequencies $h(x)$, and the Shannon entropy is given by

$$h(I) = -\sum_{x \in R(I)} p_I(x)\ln(p_I(x)) \tag{14}$$

with

$$p_I(x) = \frac{h(x)}{N_I}$$
$$N_I : \text{number of voxels in I.} \tag{15}$$

It describes the amount of information given by the intensity of an image point, the uncertainty about the intensity at a given point and the dispersion of the probabilities with which intensity values are observed [77]. Applied to the joint histogram of two images I_R, I_F the Shannon entropy thus provides a measure for their similarity (16)

$$h(I_R, I_F) = \sum_{x_R \in R(I_R)}$$
$$\sum_{x_F \in R(I_F)} p_{RF}(x_R, x_F)\ln(p_{RF}(x_R, x_F)). \tag{16}$$

As only the co-occurrence of two intensities is considered but not their difference, similarity measures based on the joint histogram are well-suited for the registration of images depicting similar objects with different intensity values. Normalized mutual information is formulated as shown in (17). Studholme *et al.* [30] have shown that the proposed integration of the marginal entropies of I_R' and I_F', respectively, provides more robustness respecting changes of the inspected overlapping regions due to the transformation

$$\mathrm{NMI}(I_R', I_F') = \frac{h(I_R') + h(I_F')}{h(I_R', I_F')}. \tag{17}$$

2) Transformations for Motion Correction: The motion correction is performed in 2-D with a combination of affine transformations and B-Spline transformations

$$\begin{pmatrix} x_{t1} \\ y_{t1} \end{pmatrix} = \underbrace{\begin{pmatrix} \cos(\alpha) & \sin(\alpha) \\ -\sin(\alpha) & \cos(\alpha) \end{pmatrix}}_{\text{Rotation}}$$
$$\times \underbrace{\begin{pmatrix} 1 & 0 \\ s & 1 \end{pmatrix}}_{\text{Shearing}} \begin{pmatrix} x \\ y \end{pmatrix} + \underbrace{\begin{pmatrix} t_x \\ t_y \end{pmatrix}}_{\text{Translation}} \tag{18}$$

$$\begin{pmatrix} x_{t2} \\ y_{t2} \end{pmatrix} = \sum_j \sum_i \begin{pmatrix} \alpha_{ij} \\ \beta_{ij} \end{pmatrix} \underbrace{B_i(x_{t1})B_j(y_{t1})}_{\text{Cubic B-Spline-Functions}} \tag{19}$$

These transformations are defined by a parameter vector $X = \{XA, XB\}$. XA defines the parameters of the affine transformation as shown in (18). After the affine transformation additional deformations can be defined by using *B*-spline transformations. For the motion correction we use a relatively coarse regular grid of 4×4 control points to define the deformation (Fig. 22). The corresponding parameters are defined by the parameter set XB.

B. Fitting of Rayleigh–Gaussian Mixture Model With Expectation Maximization

The Rayleigh–Gaussian mixture fit is a special case of fitting two probability distributions to a given set of observations. Generally, the problem can be formulated as the task of maximizing the likelihood of a given set of observations $X = \{x_1, \ldots, x_N\}$ with frequencies $h(x)$ by optimizing the parameters of the applied mixture model. Assuming that we have a set of two classes $C = \{c_R, c_G\}$ with a corresponding parameter set $\Omega = \{\theta_R, \theta_G\}$ that defines the fitted distributions, the likelihood to optimize is

$$L(\Omega|X, C) = \ln\left(\prod_{x \in X} p(x, C|\Omega)^{h(x)}\right)$$

and the expected log-likelihood can be formulated as follows:

$$E_c[\ln(L)] = E_c\left[\ln\left(\prod_{x \in X} p(x, C|\Omega)^{h(x)}\right)\bigg| x\right]$$
$$= E_c\left[\sum_{x \in X} h(x)\ln(p(x, C|\Omega))\bigg| x\right]$$
$$= \sum_{x \in X} h(x)E_c[\ln(p(x, C|\Omega)))]$$
$$= \sum_{x \in X} h(x)\sum_{c \in C} p(c|x, \Omega)\ln(p(x|c, \Omega)p(c|\Omega)).$$

We replace $p(x|c, \Omega)$ by the formulae of the Rician and Gaussian distribution and rewrite the class probabilities $p(c|\Omega)$ as variables α_R, α_G

$$E_c = \sum_{x \in X} h(x)\left(p(c_R|x, \Omega)\ln\left(\alpha_R\frac{x}{\sigma_R}e^{-\frac{x^2}{2\sigma_R^2}}\right)\right.$$
$$\left. + p(c_G|x, \Omega)\ln\left(\alpha_G\frac{1}{\sqrt{2\pi}\sigma_G}e^{\frac{1}{2}\left(\frac{x-\mu_G}{\sigma_G}\right)^2}\right)\right).$$

To maximize $E_c[\ln(L(\Omega|X,C))]$ we calculate the partial derivatives with respect to the variables $\sigma_R, \mu_G, \sigma_G, \alpha_R, \alpha_G$ assuming $\alpha_R + \alpha_G = 1$

$$\frac{\partial}{\partial \sigma_R} E_c = \frac{1}{\sigma_R} \sum_{x \in X} h(x) p(c_R|x,\Omega) \left(\left(\frac{x}{\sigma_R}\right)^2 - 2 \right)$$

$$\frac{\partial}{\partial \mu_G} E_c = \frac{1}{\sigma_G} \sum_{x \in X} h(x) p(c_G|x,\Omega)(\mu_g - x)$$

$$\frac{\partial}{\partial \sigma_G} E_c = \frac{1}{\sigma_G} \sum_{x \in X} h(x) p(c_G|x,\Omega) \left(\left(\frac{x - \mu_G}{\sigma_G}\right)^2 - 1 \right)$$

$$\frac{\partial}{\partial \alpha_i} E_c = \frac{1}{\alpha_i} \sum_{x \in X} h(x) p(c_i|x,\Omega)$$
$$- \frac{1}{1 - \alpha_i} \sum_{x \in X} h(x) p(c_i|x,\Omega), i,j \in \{R,G\}, i \neq j.$$

The formulae for the *Maximization*-step are deduced by setting these partial derivatives to 0

$$\alpha_R^{j+1} = \frac{\sum_{x \in X} h(x) p(c_R|x,\Omega^j)}{\sum_{x in X} h(x)}$$

$$\sigma_R^{j+1 2} = \frac{\sum_{x \in X} h(x) p(c_R|x,\Omega^j) x^2}{2 \sum_{x in X} h(x) p(c_R|x,\Omega^j)}$$

$$\alpha_G^{j+1} = \frac{\sum_{x \in X} h(x) p(c_G|x,\Omega^j)}{\sum_{x in X} h(x)}$$

$$\mu_G^{j+1} = \frac{\sum_{x \in X} h(x) p(c_G|x,\Omega^j) x}{\sum_{x in X} h(x) p(c_R|x,\Omega^j)}$$

$$\sigma_G^{j+1 2} = \frac{\sum_{x \in X} h(x) p(c_G|x,\Omega^j) \left(x - \mu_G^{j+1}\right)^2}{\sum_{x in X} h(x) p(c_R|x,\Omega^j)}.$$

The values for $p(c_i|x,\Omega^j), x \in X$ are calculated in the *Expectation*-step as follows:

$$p(c_R|x,\Omega^j) = \frac{\alpha_R \frac{x}{\sigma_R^2} e^{-\frac{1}{2}\left(\frac{x}{\sigma_R}\right)^2}}{\alpha_R \frac{x}{\sigma_R^2} e^{-\frac{1}{2}\left(\frac{x}{\sigma_R}\right)^2} + \alpha_G \frac{1}{\sqrt{2\pi}\sigma_G} e^{-\frac{1}{2}\left(\frac{x-\mu_G}{\sigma_G}\right)^2}}$$
$$= \frac{p_R(x)}{p_R(x) + p_G(x)}$$

$$p(c_G|x,\Omega^j) = \frac{\alpha_G \frac{1}{\sqrt{2\pi}\sigma_G} e^{-\frac{1}{2}\left(\frac{x-\mu_G}{\sigma_G}\right)^2}}{\alpha_R \frac{x}{\sigma_R^2} e^{-\frac{1}{2}\left(\frac{x}{\sigma_R}\right)^2} + \alpha_G \frac{1}{\sqrt{2\pi}\sigma_G} e^{-\frac{1}{2}\left(\frac{x-\mu_G}{\sigma_G}\right)^2}}$$
$$= \frac{p_G(x)}{p_R(x) + p_G(x)}.$$

Other than the Gaussian distribution, which can be centered around arbitrary points defined through μ_G, the offset of the Rician distribution is fixed at the origin and the parameter σ_R defines the shape (Fig. 25). The myocardial tissue intensity values are normally higher than 0 and thus we introduce an offset x_s for the mixture model

$$x_s = \arg\max_{h(x) < 0.05 h_{\max}} x.$$

The algorithm can then be implemented as shown in Fig. 26.
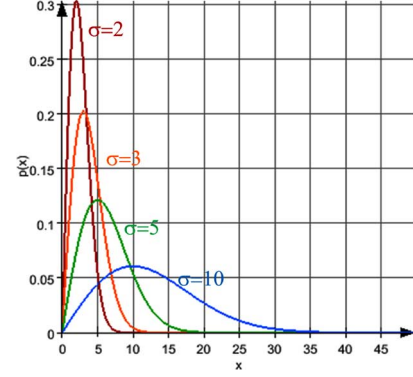

Fig. 25. Examples for the Rayleigh distribution $\alpha_R(x)/(\sigma_R^2) e^{-(1)/(2)((x)/(\sigma_R))^2}$ with parameters $\sigma_R = 2, 3, 5, 10$.

Parameter Initialization:

$$x_s = \arg\max_{x \in \{x_i | h(x_i) < 0.05 h_{max}\}} x$$

$$\sigma_R^0 = \arg\max_{x \in X} h(x - x_s)$$

$$\alpha_R^0 = \max_{x \in X} h(x)$$

$$\mu_G^0 = \sigma_R^0 + \frac{1}{2} \left(x_{max} - \arg\max_{x \in X} h(x) \right)$$

$$\sigma_G^0 = \sqrt{\frac{1}{3} (x_{max} - \mu_G^0)}$$

$$\alpha_G^0 = h(\mu_G^0) \sqrt{2\pi} \sigma_G^0$$

Iterative Expectation-Maximization until convergence:

1) **Expectation-Step:**

$$p(c_R|x,\Omega^j) = \frac{p_R(x)}{p_R(x) + p_G(x)}$$

$$p(c_G|x,\Omega^j) = \frac{p_G(x)}{p_R(x) + p_G(x)}$$

2) **Maximization-Step:**

$$\alpha_R^{j+1} = \frac{\sum_{x+x_s \in X} h(x+x_s) p(c_R|x,\Omega^j)}{\sum_{x+x_s \in X} h(x+x_s)}$$

$$\sigma_R^{j+1 2} = \frac{\sum_{x+x_s \in X} h(x+x_s) p(c_R|x,\Omega^j) x^2}{2 \sum_{x+x_s \in X} h(x+x_s) p(c_R|x,\Omega^j)}$$

$$\alpha_G^{j+1} = \frac{\sum_{x+x_s \in X} h(x+x_s) p(c_G|x,\Omega^j)}{\sum_{x+x_s \in X} h(x+x_s)}$$

$$\mu_G^{j+1} = \frac{\sum_{x+x_s \in X} h(x+x_s) p(c_G|x,\Omega^j) x}{\sum_{x+x_s \in X} h(x+x_s) p(c_R|x,\Omega^j)}$$

$$\sigma_G^{j+1 2} = \frac{\sum_{x+x_s \in X} h(x+x_s) p(c_G|x,\Omega^j)(x - \mu_G^{j+1})^2}{\sum_{x+x_s \in X} h(x+x_s) p(c_R|x,\Omega^j)}$$

Fig. 26. Expectation-maximization algorithm for fitting the Rayleigh–Gaussian mixture model to an intensity histogram $h(x)$.

rithms within the development platform MeVisLab. The authors would also like to thank G. Prause and S. Wirtz for proofreading and discussions as well as C. Claussen for supporting this work.

REFERENCES

[1] R. W. Nesto and G. J. Kowalchuk, "The ischemic cascade: Temporal sequence of hemodynamic, electrocardiographic and symptomatic expressions of ischemia," *Am. J. Cardiol.*, vol. 59, no. 7, pp. 23–30, 1987.

[2] L. G. Futterman and L. Lemberg, "Hibernating myocardium, stunning, ischemic preconditioning: Clinical relevance," *Am. J. Critical Care*, vol. 9, no. 6, pp. 430–436, 2000.

[3] R. Kim, D. Fieno, T. Parrish, K. Harris, E. L. Chen, O. Simonetti, J. Bundy, J. Finn, F. Klocke, and R. Judd, "Relationship of mri delayed contrast enhancement to irreversible injury, infarct age, and contractile function," *Circulation*, vol. 100, no. 19, pp. 1992–2002, 1999.

[4] M. Saeed, G. Lund, M. F. Wendland, J. Bremerich, H. Weinmann, and C. B. Higgins, "Magnetic resonance characterization of the peri-infarction zone of reperfused myocardial infarction with necrosis-specific and extracellular nonspecific contrast media," *Circulation*, vol. 103, no. 6, pp. 871–876, 2001.

[5] A. Yan, A. Shayne, K. Brown, S. N. Gupta, C. Chan, T. Luu, M. Carli, H. Reynolds, W. Stevenson, and R. Kwong, "Characterization of the peri-infarct zone by contrast-enhanced cardiac magnetic resonance imaging is a powerful predictor of post-myocardial infarction mortality," *Circulation*, vol. 114, no. 1, pp. 32–39, 2006.

[6] M. Tsukiji, P. Nguyen, G. Narayan, J. Hellinger, F. Chan, R. Herfkens, J. M. Pauly, M. V. McConnell, and P. C. Yang, "Peri-infarct ischemia determined by cardiovascular magnetic resonance evaluation of myocardial viability and stress perfusion predicts future cardiovascular events in patients with severe ischemic cardiomyopathy," *J. Cardiovasc. Magn. Reson.*, vol. 8, no. 6, pp. 773–779, 2006.

[7] M. Cerqueira, N. Weissman, V. Dilsizian, A. Jacobs, S. Kaul, W. Laskey, D. Pennell, J. Rumberger, T. Ryan, and M. Verani, "Standardized myocardial segmentation and nomenclature for tomographic imaging of the heart: A statement for healthcare professionals from the cardiac imaging committee of the council on clinical cardiology of the american heart association," *Circulation*, vol. 105, no. 4, pp. 539–542, 2002.

[8] O. Pereztol-Valdes, J. Candell-Riera, C. Santana-Boado, J. Angel, S. Aguade-Bruix, J. Castell-Conesa, E. V. Garcia, and J. Soler-Soler, "Correspondence between left ventricular 17 myocardial segments and coronary arteries," *Eur. Heart J.*, vol. 26, no. 24, pp. 2637–2643, 2005.

[9] X. Liu, X. Zhao, J. Huang, C. J. Francois, D. Tuite, X. Bi, D. Li, and J. C. Carr, "Comparison of 3D free-breathing coronary MR angiography and 64-MDCT angiography for detection of coronary stenosis in patients with high calcium scores," *Am. J. Roentgenol.*, vol. 189, no. 6, pp. 1326–1332, 2007.

[10] H. Arheden, M. Saeed, C. B. Higgins, D. W. Gao, J. Bremerich, R. Wyttenbach, M. W. Dae, and M. F. Wendland, "Measurement of the distribution volume of gadopentetate dimeglumine at echo-planar mr imaging to quantify myocardial infarction: Comparison with 99mtc-dtpa autoradiography in rats," *Radiology*, vol. 211, no. 3, pp. 698–708, 1999.

[11] H. Arheden, M. Saeed, C. B. Higgins, D. W. Gao, P. C. Ursell, J. Bremerich, R. Wyttenbach, M. W. Dae, and M. F. Wendland, "Reperfused rat myocardium subjected to various durations of ischemia: Estimation of the distribution volume of contrast material with echo-planar mr imaging," *Radiology*, vol. 215, no. 2, pp. 520–528, 2000.

[12] M. A. Griswold, P. M. Jakob, R. M. Heidemann, M. Nittka, V. Jellus, J. Wang, B. Kiefer, and A. Haase, "Generalized autocalibrating partially parallel acquisitions (GRAPPA)," *Magn. Reson. Med.* vol. 47, no. 6, pp. 1202–1210, Jun. 2002.

[13] J. Lötjönen, M. Pollari, S. Kivisto, and K. Lauerma, "Correction of movement artifacts from 4-D cardiac short-and long-axis MR data," in *Proc. 7th Int. Conf. Med. Image Computing Computer-Assisted Intervent. (MICCAI'04)*, 2004, pp. 405–412.

[14] J. Barajas, K. Caballero, J. Garcia-Barnes, F. Carreras, S. Pujadas, and P. Radeva, "Correction of misalignment artifacts among 2-D cardiac MR images in 3-D space," in *First International Workshop on Computer Vision for Intravascular and Intracardiac Imaging, Miccai 2006*, G. Unal, I. A. Kakadiaris, G. Slabaugh, and A. Tannenbaum, Eds., 2006, vol. 1, pp. 114–121.

[15] L. Bidaut and J. Vallee, "Automated registration of dynamic MR images for the quantification of myocardial perfusion," *J. Mag. Reson. Imag.*, vol. 13, no. 4, pp. 648–655, 2001.

[16] M. Breeuwer, L. Spreeuwers, and M. Quist, "Automatic quantitative analysis of cardiac MR perfusion images," *Proc. SPIE*, vol. 4322, p. 733, 2004.

[17] S. Gupta, M. Solaiyappan, G. Beache, A. Arai, and T. Foo, "Fast method for correcting image misregistration due to organ motion in time-series MRI data," *Magn. Reson. Med.*, vol. 49, no. 3, pp. 506–514, 2003.

[18] R. Bansal and G. Funka-Lea, "Integrated image registration for cardiac MR perfusion data," in *Proc. 5th Int. Conf. Med. Image Computing Computer-Assisted Intervent. (MICCAI'02)*, 2002, pp. 659–666.

[19] L. Bracoud, F. Vincent, C. Pachai, E. Canet, P. Croisille, and D. Revel, "Automatic registration of MR first-pass myocardial perfusion images," in *Proc. 2nd Int. Workshop Functional Imag. Model. Heart*, 2003, pp. 215–223.

[20] Y. Sun, M. Jolly, and J. Moura, "Contrast-invariant registration of cardiac and renal MR perfusion images," in *Proc. 7th Int. Conf. Med. Image Computing Computer-Assisted Intervention (MICCAI'04)*, 2004, pp. 903–910.

[21] C. Gallippi and G. Trahey, "Automatic image registration for MR and ultrasound cardiac images," in *Proc. 17th Int. Conf. Inf. Process. Med. Imag. (IPMI'01)*, 2001, pp. 141–147.

[22] M. Stegmann, H. Ólafsdóttir, and H. Larsson, "Unsupervised motion-compensation of multi-slice cardiac perfusion MRI," *Med. Image Anal.*, vol. 9, no. 4, pp. 394–410, 2005.

[23] A. Discher, N. Rougon, and F. Preteux, "An unsupervised approach for measuring myocardial perfusion in MR image sequences," *Proc. SPIE*, vol. 5916, p. 59160C, 2005.

[24] N. Rougon, A. Discher, and F. Preteux, "Region-driven statistical non-rigid registration: Application to model-based segmentation and tracking of the heart in perfusion MRI," *Proc. SPIE*, vol. 5916, p. 59160E, 2005.

[25] M. Breeuwer, I. Paetsch, E. Nagel, R. Muthupillai, S. Flamm, and S. Plein, "The detection of normal, ischemic and infarcted myocardial tissue using MRI," in *Proc. 17th Int. Congress Exhibit. Comput. Assist. Radiol. Surg. (CARS'03)*, 2003, pp. 1153–1158.

[26] C. Swingen, R. T. Seethamraju, and M. Jerosch-Herold, "An approach to the three-dimensional display of left ventricular function and viability using MRI," *Int. J. Cardiovasc. Imag.*, vol. 19, no. 4, pp. 325–336, 2003.

[27] B. Sturm, K. A. Powell, and A. E. Stillman, "Registration of 3D CT angiography and cardiac MR images in coronary artery disease patients," *Int. J. Cardiovasc. Imag.*, vol. 19, no. 4, pp. 281–293, 2003.

[28] R. Setser, T. O'Donnell, N. Smedira, J. Sabik, S. Halliburton, A. Stillman, and R. White, "Coregistered MR imaging myocardial viability maps and multi-detector row CT coronary angiography displays for surgical revascularization planning: Initial experience," *Radiology*, vol. 237, no. 2, pp. 465–473, 2005.

[29] R. Smolíková-Wachowiak, M. Wachowiak, A. Fenster, and M. Drangova, "Registration of two-dimensional cardiac images to preprocedural three-dimensional images for interventional applications," *J. Magn. Reson. Imag.*, vol. 22, no. 2, pp. 219–228, 2005.

[30] C. Studholme, D. Hill, D. , and Hawkes, "An overlap invariant entropy measure of 3D medical image alignment," *Pattern Recogniti.*, vol. 32, pp. 71–86, 1999.

[31] J. Nelder and R. Mead, "A simplex method for function minimization," *Comput. J.*, vol. 7, no. 4, pp. 308–313, 1965.

[32] W. J. Rogers, E. P. Shapiro, J. L. Weiss, M. B. Buchalter, F. E. Rademakers, M. L. Weisfeldt, and E. A. Zerhouni, "Quantification of and correction for left ventricular systolic long-axis shortening by magnetic resonance tissue tagging and slice isolation," *Circulation*, vol. 84, no. 2, pp. 721–731, 1991.

[33] A. Frangi, W. Niessen, R. Hoogeveen, T. van Walsum, and M. Viergever, "Model-based quantitation of 3-D magnetic resonance angiographic images," *IEEE Trans. Med. Imag.*, vol. 18, no. 10, pp. 946–956, Oct. 1999.

[34] J. Suri, K. Liu, L. Reden, and S. Laxminarayan, "A review on MR vascular image processing algorithms: Acquisition and prefiltering: Part I," *IEEE Trans. Inf. Technol. Biomed.*, vol. 6, no. 4, pp. 324–337, Dec. 2002.

[35] A. Frangi, W. Niessen, K. Vincken, and M. Viergever, "Multiscale vessel enhancement filtering," in *Proc. 1st Int. Conf. Med. Image Computing Computer-Assisted Intervent. (MICCAI'98)*, 1998, pp. 130–137.

[36] P. Soille and H. Talbot, "Directional morphological filtering," *IEEE Trans. Pattern Anal. Mach. Intell.*, vol. 23, no. 11, pp. 1313–1329, Nov. 2001.

[37] D. Selle, B. Preim, A. Schenk, and H. Peitgen, "Analysis of vasculature for liver surgical planning," *IEEE Trans. Med. Imag.*, vol. 21, no. 11, pp. 1344–1357, Nov. 2002.

[38] F. Quek and C. Kirbas, "Vessel extraction in medical images by wave-propagation and traceback," *IEEE Trans. Med. Imag.*, vol. 20, no. 2, pp. 117–131, Feb. 2001.

[39] B. Avants and J. Williams, "An adaptive minimal path generation technique for vessel tracking in CTA/CE-MRA volume images," in *Proc. 4th Int. Conf. Med. Image Comput. Computer-Assisted Intervent. (MICCAI'01)*, 2001, pp. 707–716.

[40] M. Hernandez-Hoyos, A. Anwander, M. Orkisz, J. Roux, P. Douek, and I. Magnin, "A deformable vessel model with single point initialization for segmentation, quantification and visualization of blood vessels in 3D MRA," in *Proc. 3rd Int. Conf. Med. Image Comput. Computer-Assisted Intervent. (MICCAI'00)*, 2000, pp. 735–744.

[41] C. Lorenz, S. Renisch, T. Schlathoelter, and T. Buelow, "Simultaneous segmentation and tree reconstruction of the coronary arteries in MSCT images," *Proc. SPIE*, vol. 5031, p. 167, 2003.

[42] S. Wesarg and E. Firle, "Segmentation of vessels: The corkscrew algorithm," *Proc. SPIE*, vol. 5370, pp. 1609–1620, 2004.

[43] A. Hennemuth, S. Bock, T. Boskamp, D. Fritz, C. Kuehnel, D. Rinck, and M. Scheuering, "One-click coronary tree segmentation in CT angiographic images," in *Proc. 19th Int. Congress Exhibit. Comput. Assist. Radiol. Surg. (CARS'05)*, 2005, pp. 317–321.

[44] J. Keegan, P. Horkaew, T. Buchanan, T. Smart, G. Yang, and D. Firmin, "Intra-and interstudy reproducibility of coronary artery diameter measurements in magnetic resonance coronary angiography," *J. Magn. Reson. Imag.*, vol. 20, no. 1, pp. 160–166, 2004.

[45] A. Kolipaka, G. Chatzimavroudis, R. White, T. O'Donnell, and R. Setser, "Segmentation of non-viable myocardium in delayed enhancement magnetic resonance images," *Int. J. Cardiovasc. Imag.*, vol. 21, no. 2–3, pp. 303–311, 2005.

[46] V. Positano, A. Pingitore, A. Giorgetti, B. Favilli, M. Santarelli, L. Lan-dini, P. Marzullo, and M. Lombardi, "A fast and effective method to assess myocardial necrosis by means of contrast magnetic resonance imaging," *J. Cardiovascular Magn. Reson.*, vol. 7, no. 2, pp. 487–494, 2005.

[47] T. O'Donnell, N. Xu, R. Setser, and R. White, "Semi-automatic segmentation of nonviable cardiac tissue using cine and delayed enhancement magnetic resonance images," *Proc. SPIE*, vol. 5031, p. 242, 2003.

[48] K. A. Reimer and R. B. Jennings, "The "wavefront phenomenon" of myocardial ischemic cell death. II. transmural progression of necrosis within the framework of ischemic bed size (myocardium at risk) and collateral flow," *Lab. Invest.*, vol. 40, no. 6, pp. 633–644, Jun. 1979.

[49] L. Hsu, A. Natanzon, P. Kellman, G. Hirsch, A. Aletras, and A. Arai, "Quantitative myocardial infarction on delayed enhancement MRI, Part I: Animal validation of an automated feature analysis and combined thresholding infarct sizing algorithm," *J. Magn. Reson. Imag.*, vol. 23, pp. 298–308, 2006.

[50] D. Saering, J. Ehrhardt, A. Stork, P. Bansmann, G. Lund, and H. Han-dels, "Analysis of the left ventricle after myocardial infarction combining 4D cine-MR and 3d DE-MR image sequences," in *Bild-verarbeitung fuer die Medizin 2006, Informatik Aktuell*, 2006, pp. 56–60.

[51] K. Choi, R. Kim, G. Gubernikoff, J. Vargas, M. Parker, and R. Judd, "Transmural extent of acute myocardial infarction predicts long-term improvement in contractile function," *Circulation*, vol. 104, no. 10, pp. 1101–1107, 2001.

[52] N. Noble, D. Hill, M. Breeuwer, and R. Razavi, "The automatic identification of hibernating myocardium," in *Proc. 7th Int. Conf. Med. Image Computing Computer-Assisted Intervent. (MICCAI'04)*, 2004, pp. 890–898.

[53] V. Positano, M. Santarelli, A. Pingitore, M. Lombardi, L. Landini, and A. Benassi, "Quantitative 3D assessment of myocardial viability with MRI delayed contrast enhancement," in *Proc. 30th Annu. Conf. Comput. Cardiol. (CARS'03)*, 2003, pp. 629–632.

[54] J. Schwitter, "Myocardial perfusion," *J. Magn. Reson. Imag.*, vol. 24, no. 5, pp. 953–963, 2006.

[55] N. Al Saadi, M. Gross, A. Bornstedt, B. Schnackenburg, C. Klein, E. Fleck, and E. Nagel, "Comparison of various parameters for determining an index of myocardial perfusion reserve in detecting coronary stenosis with cardiovascular magnetic resonance tomography," *Z. Kardiol.*, vol. 90, no. 11, pp. 824–834, 2001.

[56] J. T. Keijer, A. C. van Rossum, M. J. van Eenige, A. J. Karreman, M. B. Hofman, J. Valk, and C. A. Visser, "Semiquantitation of regional myocardial blood flow in normal human subjects by first-pass magnetic resonance imaging," *Am. Heart J.*, vol. 130, no. 4, pp. 893–901, 1995.

[57] F. Klocke, O. Simonetti, R. Judd, R. Kim, K. Harris, S. Hedjbeli, D. Fieno, S. Miller, V. Chen, and M. Parker, "Limits of detection of regional differences in vasodilated flow in viable myocardium by first-pass magnetic resonance perfusion imaging," *Circulation*, vol. 104, no. 20, pp. 2412–2416, 2001.

[58] M. Schmitt, O. Mohrs, S. Petersen, K. Kreitner, T. Voigtlander, T. Wittlinger, G. Horstick, S. Ziegler, J. Meyer, M. Thelen, and W. Schreiber, "Evaluation of myocardial perfusion reserve in patients with cad using contrast-enhanced MRI: A comparison between semiquantitative and quantitative methods," *Rofo-Fortschr. Roentgenstr.*, vol. 174, no. 2, pp. 187–195, 2002.

[59] E. J. Sainsbury and J. J. Ashley, "Curve-fitting in pharmacokinetics-a comparison between gamma- and biexponential fits," *Eur. J. Clin. Pharmacol.*, vol. 30, no. 2, pp. 243–244, 1986.

[60] H. K. Thompson, C. F. Starmer, R. E. Whalen, and H. D. McIntosh, "Indicator transit time considered as a gamma variate," *Circ. Res.*, vol. 14, pp. 502–515, 1964.

[61] N. Al Saadi, M. Gross, I. Paetsch, B. Schnackenburg, A. Bornstedt, E. Fleck, and E. Nagel, "Dobutamine induced myocardial perfusion reserve index with cardiovascular MR in patients with coronary artery disease," *J. Cardiovascular Magn. Reson.*, vol. 4, no. 4, pp. 471–480, 2002.

[62] V. Positano, A. Pingitore, B. Scattini, M. F. Santarelli, D. D. Marchi, B. Favilli, M. Lombardi, and L. Landini, "Myocardial perfusion by first pass contrast magnetic resonance: A robust method for quantitative regional assessment of perfusion reserve index," *Heart*, vol. 92, no. 5, pp. 689–690, 2006.

[63] V. Positano, M. Santarelli, and L. Landini, "Automatic characterization of myocardial perfusion in contrast enhanced MRI," *EURASIP J. Appl. Signal Process.*, vol. 2003, no. 5, pp. 413–421, 2003.

[64] E. Di Bella and A. Sitek, "Time curve analysis techniques for dynamic contrast MRI studies," in *Proc. 17th Int. Conf. Inf. Process. Med. Imag. (IPMI'01)*, 2001, pp. 211–217.

[65] M. Hansen, H. Ólafsdóttir, K. Sjöstrand, S. Erbou, M. Stegmann, H. Larsson, and R. Larsen, "Ischemic segment detection using the support vector domain description," *Proc. SPIE*, vol. 6512, p. 65120F, 2007.

[66] T. Boskamp, D. Rinck, F. Link, B. Kuemmerlen, G. Stamm, and P. Mildenberger, "New vessel analysis tool for morphometric quantification and visualization of vessels in CT and MR imaging data sets," *Radiographics*, vol. 24, no. 1, pp. 287–297, 2004.

[67] A. Hennemuth, A. Seeger, O. Friman, S. Miller, and H.-O. Peitgen, "Automatic detection and quantification of non-viable myocardium in late enhancement images," in *Proc. 16th Sci. Meeting Int. Soc. Magn. Reson. Med. (ISMRM'08)*, 2008, p. 1039.

[68] H. Gudbjartsson and S. Patz, "The Rician distribution of noisy MRI data," *Magn. Reson. Med.*, vol. 34, no. 6, pp. 910–914, 1995.

[69] A. Schenk, G. Prause, and H.-O. Peitgen, "Efficient semiautomatic segmentation of 3D objects in medical images," in *Proc. 3rd Int. Conf. Med. Image Computing Computer-Assisted Intervent. (MICCAI'00)*, 2000, pp. 186–195.

[70] H. Akaike, "Information theory and an extension of the maximum likelihood principle," in *Second International Symposium on Information Theory*, B. N. Petrov and B. F. Csaki, Eds., 1973, pp. 267–281.

[71] G. Schwarz, "Estimating the dimension of a model," *Ann. Stat.*, vol. 6, no. 2, pp. 461–464, 1978.

[72] O. Friman, A. Hennemuth, and H. Peitgen, "A Rician-Gaussian mixture model for segmenting delayed enhancement MRI images," in *Proc. 16th Sci. Meeting Int. Soc. Magn. Reson. Med. (ISMRM'08)*, 2008, p. 1040.

[73] H. van Assen, M. Danilouchkine, A. Frangi, S. Ordás, J. Westenberg, J. Reiber, and B. Lelieveldt, "SPASM: A 3D-ASM for segmentation of sparse and arbitrarily oriented cardiac MRI data," *Med. Image Anal.*, vol. 10, no. 2, pp. 286–303, 2006.

[74] L. Spreeuwers and M. Breeuwer, "Automatic detection of myocardial boundaries in mr cardio perfusion images," in *Proc. 4th Int. Conf. Med. Image Computing Computer-Assisted Intervent. (MICCAI'01)*, 2001, pp. 1228–1231.

[75] C. Ciofolo, M. Fradkin, B. Mory, G. Hautvast, and M. Breeuwer, "Automatic myocardium segmentation in late-enhancement MRI," in *Proc. 5th IEEE Int. Symp. Biomed. Imag.: From Nano Macro ISBI 2008*, 2008, pp. 225–228.

[76] C. Shannon, "A mathematical theory of communication," *Bell Syst. Tech. J.*, vol. 27, pp. 379, 323–656, 423, 1948.

[77] J. P. W. Pluim, J. B. A. Maintz, and M. A. Viergever, "Mutual-information-based registration of medical images: A survey," *IEEE Trans. Med. Imag.*, vol. 22, no. 8, pp. 986–1004, Aug. 2003.